Estuaries and Coasts
https://doi.org/10.1007/s12237-020-00844-8

Nonlinear Interaction Between the Tide and the Storm Surge with the Current due to the River Flow in the Río de la Plata

Matías G. Dinápoli[1,2,3,4] · **Claudia G. Simionato**[1,2,3,5] · **Diego Moreira**[1,2,3,5]

Received: 3 February 2020 / Revised: 24 September 2020 / Accepted: 28 September 2020

Abstract

The Río de la Plata estuary (RdP) is characterized by the large flow of its tributary rivers (Q), with an average of 22,000 m^3 s^{-1} and an interannual variability range from 8000 to 90,000 m^3 s^{-1}. In this work, the hypothesis that the current due to that flow (CDR) interacts nonlinearly with both the tides and storm surges is evaluated utilizing water level observations and numerical simulations. Two tide gauge time series gathered at the freshwater tidal zone (FTZ) of the RdP are analyzed with the novel surrogate analysis. The analysis is applied for periods of high, medium and low Q. Results show that both interactions occur at the upper half of the FTZ and increase with Q. Harmonic analyses support the surrogate analysis' conclusions and show that tide-CDR interaction redistributes the energy among tidal harmonics, increasing asymmetry. Numerical simulations confirm that (i) both interactions maximize at the upper half of the FTZ and decrease downstream; and (ii) they are modulated by Q; a rise of about 14,000 m^3 s^{-1} (interquartile range) can produce an intensification of 50% and 100% of the amplitudes of the tide-CDR and surge-CDR interactions, respectively; and (iii) both interactions introduce asymmetries in the water level, with faster rises and slower falls; (iv) the quadratic bottom friction is the main source of both interactions; (v) tide-CDR interaction represents 12% of the water level associated with the tide, whereas surge-CDR interaction accounts for 5% of the surge peak; and (vi) the interactions are significant in the upper FTZ because there, the magnitude of the currents associated with the tide and the surge are comparable to CDR; downstream, the channel widens and CDR decreases.

Keywords Tide-river flow interaction · Surge-river flow interaction · Río de la Plata estuary · Storm surge modeling · Storm surge forecast

Communicated by Arnoldo Valle-Levinson

✉ Matías G. Dinápoli
matias.dinapoli@cima.fcen.uba.ar

[1] Facultad de Ciencias Exactas y Naturales, Universidad de Buenos Aires, Pabellón II - 2do, Piso Ciudad Autónoma de Buenos Aires, Argentina

[2] Centro de Investigaciones del Mar y la Atmósfera (CIMA), CONICET - Universidad de Buenos Aires, Pabellón II - 2do, Piso Ciudad Autónoma de Buenos Aires, Argentina

[3] CNRS - IRD - CONICET - UBA, Instituto Franco-Argentino para el Estudio del Clima y sus Impactos (UMI 3351 IFAECI), Pabellón II - 2do, Piso Ciudad Autónoma de Buenos Aires, Argentina

[4] Intendente Güiraldes 2160 (Ciudad Universitaria), Pabellón II - 2do, Piso Ciudad Autónoma de Buenos Aires, Argentina

[5] Departamento de Ciencias de la Atmósfera y los Océanos, Facultad de Ciencias Exactas y Naturales, Universidad de Buenos Aires, Pabellón II - 2do, Piso Ciudad Autónoma de Buenos Aires, Argentina

Introduction

In the freshwater zone of the estuaries highly influenced by tides (hereinafter referred to as FTZ), the current due to the flow of tributary rivers (CDR) can combine with surges and tides to produce an increased risk of flooding (Maskell 2012; Spicer 2019). The problem is complex since the interactions between tides, surges and CDR in estuaries and tidal rivers are not necessarily linear (see, for instance, Hoitink and Jay 2016 and references therein) and are not fully understood yet (Cai et al. 2018; Zhang et al. 2018). The physical processes in freshwater tidal zones of estuaries were deeply discussed in the review by Hoitink and Jay (2016), where references to a number of articles on the subject can be found. Tidal propagation in those systems is the result of nonlinear interactions between ocean tides, channel geometry, bottom friction, and CDR (Matte et al. 2014), which integrally produce distortion and damping of the tidal wave as it propagates upstream (LeBlond 1978). In addition, the damping of

Published online: 09 November 2020

the tide is not a local phenomenon but is the integrated result of wave propagation through complex geometry with nonlinear effects (Guo et al. 2015). In terms of harmonic analysis, the distortion of the tide is reflected in the generation of overtides (e.g., Jay 1991; Friedrichs and Aubrey 1994; Parker 2007; Savenije et al. 2008; Luz Clara Tejedor et al. 2014; Guo et al. 2015 and references in it). Jay (1991) and Jay and Flinchem (1997) summarized that in freshwater tidal zones, the behavior of the tide is complex due to the combination of the following processes: (i) strong frictional damping by a CDR; (ii) variable interaction of barotropic tide with itself through nonlinearities in bed stresses that are modulated by a CDR; (iii) topographic funnelling of tidal waves in a predominantly convergent fluvial geometry; (iv) incident and reflected waves of each species; and (v) advection of the tide by a CDR. In particular, this last item includes the reduction of the amplitude of the tide, the delay of the propagation and even the perturbation of the energy distribution among the tidal harmonics (Godin 1985, 1991, 1999; Jay and Flinchem 1997; Horrevoets et al. 2004). Surges, which are also long waves (Gill 1982; Pedlosky 1987; Pugh 2004) also suffer nonlinear effects as they propagate through the freshwater tidal zones due to the geometry of the channel, the friction and even due to the interaction with CDR (WMO 2011).

Several studies have identified nonlinear interactions between the tide and CDR in freshwater tidal zones (e.g., Gallo and Vinzon 2005 for the Amazon, Alebregtse and de Swart 2016 for the Yangtze, Matte et al. 2014 for the St. Lawrence, Sassi and Hoitink 2013 for the Mahakam and Jay et al. 2016 for the Columbia). Regarding their impact on the tidal range, for instance (Zhang et al. 2018) found that in the estuary of the Yangtze River (China) the continental discharge can produce a variation of the tidal amplitude of approximately 12.5%.

Although many works analyzed the interaction between the surge and tides (for instance, Proudman 1955a; Doodson 1956; Rossiter 1961; Godin 1972; Wolf 1981; Murty 1984; Bijlsma 1986; Flather 2001; Bernier and Thompson 2007; Jones and Davies 2008; Dinàpoli et al. 2020c), studies on the interaction between the surge and CDR are relatively scarcer. For instance, in the Suyeong Bay (South Korea) surge-CDR interaction can increase the water level by more than 0.38 m (Kim et al. 2018). In UK estuaries, characterized by surges with amplitudes of up to 2.00 m and continental discharges of approximately 1500 $m^3\ s^{-1}$, it was found that surge-CDR interaction can increase the water level by up to 0.35 m (Maskell et al. 2013). In the Tamsui River (Taiwan) surge-CDR interaction produces changes in the water level that depend on the amplitude of the surge and the value of CDR (Maskell et al. 2016). In the Pearl River (China) it was observed that the average water level is an order of magnitude higher during the flood season than during the dry season (Cai et al. 2018). Thus, the literature suggests that the effects of surge-CDR interaction on the water level are characteristic of each site and, therefore, their understanding requires specific studies.

As far as we know, the only study dealing with these interactions in the Río de la Plata estuary (RdP) is the one by Luz Clara Tejedor et al. (2014); they found that the amplitude of the harmonic tidal constituent M_2 presents pseudo-periodic oscillations of about 10%, which correlate very well with continental freshwater discharge transported by its tributary rivers (Q) and that seems to be the result of tide-CDR interaction. To date no study has been made for the RdP yet and, therefore, the possible modifications of the surge and the impacts on its forecast are not known yet.

The aim of this work is to study the tide-CDR and surge-CDR interactions in the FTZ of the RdP, to (i) contribute to expanding knowledge about physical processes in this estuarine system, particular among others in the world because of its large width and strong flow, and (ii) improve the scientific basis for the forecasting of tides and surges in the region. The occurrence of surge-CDR and tide-CDR interactions in the FTZ of the RdP is detected on tide gauge observations; then, interactions are characterized and quantified applying process oriented numerical simulations, and the physical mechanisms that produce them are identified and discussed.

Study Area

The Río de la Plata (RdP; Fig. 1) is an extensive estuarine system located on the eastern coast of Southern South America, at approximately 35° S, that drains the waters of the second largest basin of the subcontinent, after the Amazon River (Moreira and Simionato 2019). The RdP has a freshwater zone (Meccia et al. 2013; Guerrero et al. 1997) highly influenced by tides (Simionato et al. 2004b; D'Onofrio et al. 2008), hereinafter referred to as FTZ, that extends from the mouths of the main tributary rivers (Paraná and Uruguay; Fig. 1) to the submersed Barra del Indio Shoal (Fig. 1). The bottom salinity front (Guerrero et al. 1997) and the turbidity maximum of the RdP are located downstream the shoal throughout the year (Moreira et al. 2013; Dogliotti et al. 2016); the shoal, in turn, develops because of the related sediments dynamics (Moreira and Simionato 2019). The surface salinity signal associated with the freshwater plume of the RdP can extend for many

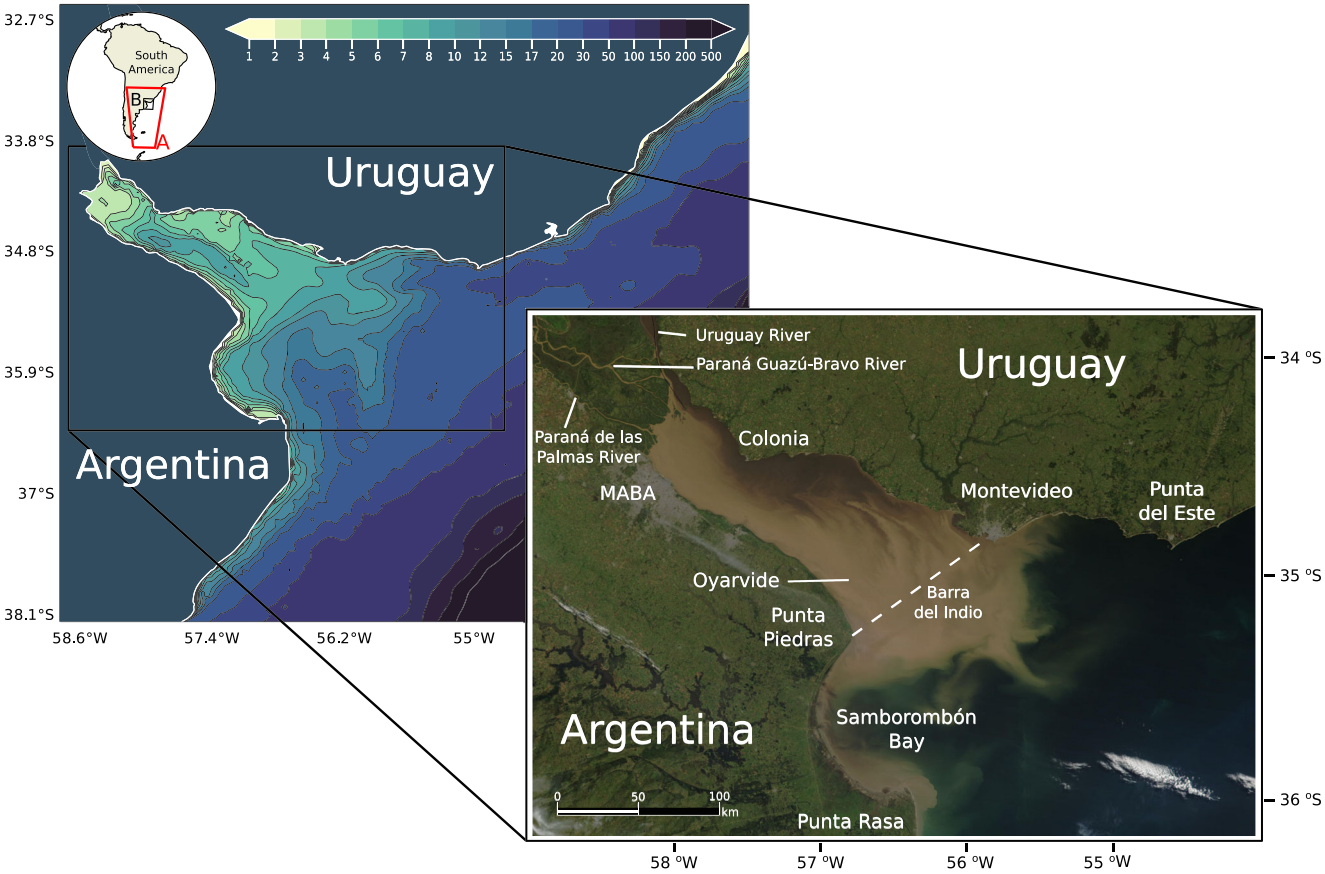

Fig. 1 Area of study, bathimetry (left panel) and geographical references (right panel). The subfigure on the left panel shows the domain of the two nested models (A and B). The image on the right panel shows data collected by the MODIS sensor aboard the Terra satellite for a period between spring and summer of 2002; adapted from https://visibleearth.nasa.gov/images/58924/rio-de-la-plata-argentina

hundreds of kilometers along the Uruguayan and Brazilian coasts (Campos et al. 1999; Piola et al. 2008; Romero 2008). This way, the area occupied by the FTZ of the RdP is well represented by the turbid region in Fig. 1. The mean depth of this area is less than 10 m (Balay 1961; Fig. 1), and extends along more than 200 km, with a width that varies from 40 km at the upper part, close to Metropolitan Area of Buenos Aires (MABA; Fig. 1), to about 110 km along the imaginary line between Punta Piedras and Montevideo (Luz Clara Tejedor et al. 2014; Fig. 1). Because of its large breadth, the FTZ has particular dynamical features (see, for instance, Simionato et al. 2004b, 2005, 2006b, 2007).

The FTZ of the RDP is very important from the ecological and socio-economic points of view. The largest cities of southern South America, including the capitals of Argentina and Uruguay (MABA and Montevideo, respectively; Fig. 1), so as a number industrial poles, harbors and resorts, are located on its coasts. As a consequence, the population of the region is very large, with approximately 16 million people just at MABA (Fig. 1). Sailing, and passengers and commodities transportation activities take place daily between Argentina, Uruguay and the countries located at the upper Plata Basin (Paraguay and Brazil), along channels that demand permanent dredging (Re et al. 2010; Santoro et al. 2011; Re and Menéndez 2011). The RdP is also the main source of drinking water for the millions of inhabitants in the region (Moreira and Simionato 2019). As a consequence of its development, the FTZ is the main focus of aquatic and atmospheric contamination, which also concentrates there (Simionato et al. 2004b).

The FTZ of the RDP is affected by strong storm surges with amplitudes that easily exceed $\pm$ 2.5 m (D'Onofrio et al. 2008) that flood MABA and disable drinking water supply during positive and negative extreme events, respectively. Therefore, the understanding and modeling of the propagation of tidal waves and storm surges in the RdP is socio-economically important, for their forecast and for the management of the drinking water supplies, the sailing channels, and the ecosystem, as in other populated estuarine systems of the world (Dronkers J 1986; Friedrichs and Aubrey 1994; Kukulka 2003; Buschman et al. 2009; Hoitink and Jay 2016).

The RdP is characterized by a large Q. The Paraná and Uruguay rivers (Fig. 1) account for about 97% of Q,

whereas the remaining 3% is transported by the minor tributaries which individual liquid discharges are two orders of magnitude less (Framiñan and Brown 1996; Framiñán et al. 1999). The long term mean Q to the RdP is 22,000 $m^3\ s^{-1}$ (Fig. 2; Jaime et al. 2002), with a relatively weak seasonal cycle (Simionato et al. 2001) but large variability on interannual timescales associated to the cycles of El Niño Southern Oscillation (ENSO; Robertson and Mechoso 1998). Extreme peaks can reach values as low as less than 10,000 $m^3\ s^{-1}$ during La Niña periods and as high as almost 90,000 $m^3\ s^{-1}$ during El Niño events (Jaime et al. 2002; Fig. 2). Q generates a downstream current (hereinafter referred to as CDR) in the FTZ that can strongly vary over time. Despite the large width of the RdP, CDR is large in the upper FTZ and weakens downstream as the channel widens and deepens (Simionato et al. 2004a). A simple estimation, dividing Q by the characteristic depth and width of the FTZ, drives to a CDR of about 0.40 ms^{-1} at the uppermost part and 0.03 ms^{-1} at the Barra del Indio Shoal for average conditions; remarkably, those values can reach 1.30 ms^{-1} and 0.10 ms^{-1}, respectively, for high Q conditions.

Methods

Data

Hourly water level observations in the RdP have been collected by the Servicio de Hidrografía Naval (SHN). In this article two stations located in the FTZ are used: Palermo (located at MABA; Fig. 1) and Oyarvide (Fig. 1), where observations over large periods of time have been gathered. Records at Palermo started in 1903 and at Oyarvide in 1980. Tide gauge levels are referred to the common Tidal Datum (0.79 m under the mean level) and all the observations were subject to a quality control using the package developed by D'Onofrio (1984).

Daily continental discharge observations were provided by the Instituto Nacional del Agua. Records at Paraná de las Palmas, Paraná Guazú-Bravo and Uruguay rivers (Fig. 1) started in 1931 and observations were subject to quality control by the institution (Borús et al. 2008).

Surrogate Analysis

The aim of the surrogates analysis is to find evidence of nonlinearities in time series, particularly for intermittent processes such as storm surges (Lancaster et al. 2018 and references therein). Surrogates are defined as a set of time series that only share all the linear properties (power spectrum and autocorrelation function) with the original time series, which can be direct observations or experimental data. The goal is to test the null hypothesis that the original time series can also be described by a linear stochastic model; thus, if this null hypothesis is rejected, there is evidence for a significant nonlinear component in the original time series (Lancaster et al. 2018 and references therein).

Following the approach of Dinápoli et al. (2020c) the Iterative Amplitude Adjusted Fourier Transform (IAAFT; Schreiber and Schmitz 1996) was chosen to analyze tide gauge series at the FTZ of the RdP. The aim of IAAFT is to generate a surrogate set with a power spectrum as close to that of the original data as possible. This way, the resulting surrogate time series will have almost the same amplitude

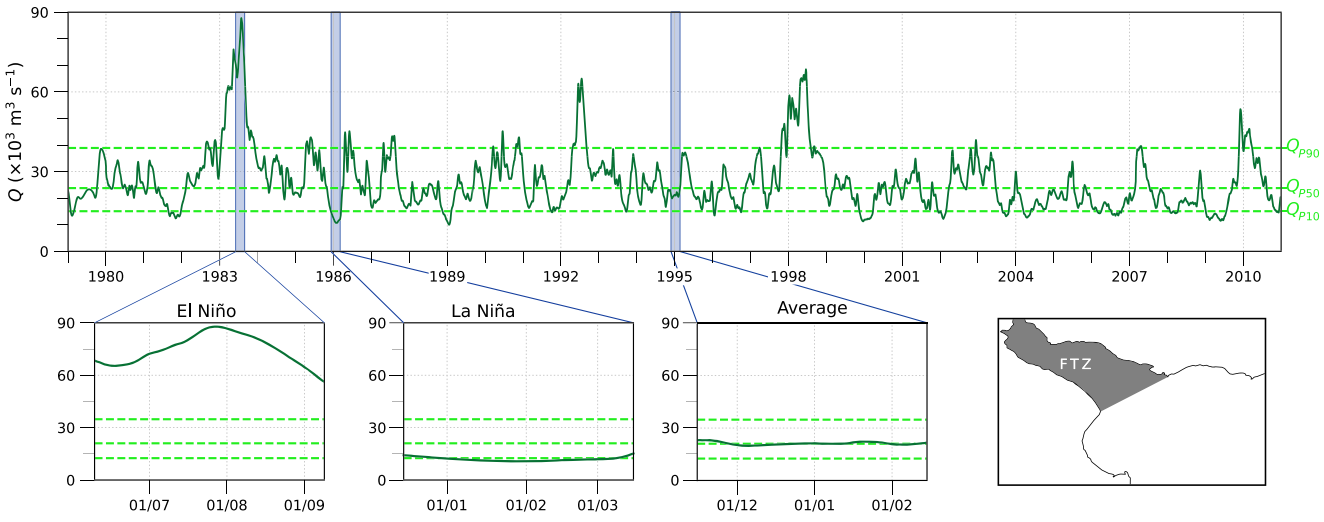

Fig. 2 Upper panel: Freshwater discharge (Q) of the RdP. Dashed lines indicate the 10th, 50th and 90th percentiles of Q (Q_{P10}, Q_{P50}, Q_{P90}, respectively). Lower panel: historical maximum and minimum extremes during El Niño (left panel) and La Niña (central panel) periods, respectively; and, an arbitrary period with average Q (right panel). The map references the area covered by the FTZ of the RdP

distribution as the original time series, but without nonlinear features. For further details on the methodology, the reader is referred to Schreiber and Schmitz (1996), Lancaster et al. (2018), and Dinàpoli et al. (2020c). The comparison between surrogate and original time series is done by calculating a nonlinear discriminating statistic. In this work the time-irreversibility (α; Lancaster et al. 2018) was chosen, defined as Eq. 1:

$$\alpha^3 = \frac{1}{T}\sum_{t=0}^{T-1}(\eta_{t+1} - \eta_t)^3 \tag{1}$$

where T is the length of the time series η_t. This score characterizes the invariance of the signal with respect to an inversion of time; α can achieve both positive and negative values, and for time-reversible signals (linear systems) it should be almost negligible. Surrogates were computed with a Python library developed by Mannattil and tested in several works, e.g., Mannattil et al. (2016), Mannattil et al. (2017), and Dinàpoli et al. (2020c).

Numerical Model and Simulations

In this study a regionalized pre-operational modeling system based on the ocean primitive equations CROCO (Coastal and Regional Ocean COmmunity model, http://www.croco-ocean.org; Debreu et al.'s 2012) numerical model was applied. The particular regionalization for the simulations of the RdP utilized in this work was implemented and validated by Dinàpoli et al. (2020b) and Dinàpoli et al. (2020a) and used for the study of tide-surge interactions by Dinàpoli et al. (2020c). CROCO was applied on a barotropic 2D version, as it is usually done to study tide-surge-river interactions in freshwater zones (e.g., Rossiter 1961; Sinha et al. 1996; Gallo and Vinzon 2005; Guo et al. 2015; Maskell et al. 2014; Cai et al. 2018; Zhang et al. 2018; Lyddon et al. 2018; Losada et al. 2017; Wankang et al. 2019; Dinàpoli et al. 2020c). The 2D barotropic model is based on the depth-averaged momentum and continuity equations as follows, Eqs. 2 and 3:

$$\frac{\partial \mathbf{u}}{\partial t} + (\mathbf{u}\cdot\nabla)\,\mathbf{u} + f\hat{z}\times\mathbf{u} = -g\nabla\eta - \frac{1}{\rho_0}\nabla p_{at} + \frac{1}{\rho_0 H}(\boldsymbol{\tau}_S - \boldsymbol{\tau}_B) \tag{2}$$

$$\frac{\partial \eta}{\partial t} + \nabla\cdot(H\mathbf{u}) = 0 \tag{3}$$

where $\mathbf{u}$ represents the depth-averaged velocity; t the time; f the Coriolis parameter; $\hat{z}$ the versor normal to the surface; g the acceleration due to gravity; η the water level; ρ_0 the water density; p_{at} the surface atmospheric pressure; H the total water depth, i.e., the addition of η and the undisturbed water depth (h); $\boldsymbol{\tau}_S$ and $\boldsymbol{\tau}_B$ surface wind and bottom friction stress tensors, respectively.

The application of CROCO used in this paper was implemented by means of two nested domains of different resolutions and scales. Model A is the lowest resolution/largest scale domain, spanning from 69° W to 46° W and from 59° S to 26° S (Fig. 1, subfigure), with horizontal zonal/meridional resolutions of 7.50′/5.25′ (equivalent to approximately 12 km). The solutions of this model are used to provide boundary conditions to a higher resolution domain focused on the RdP (Model B; Fig. 1). Model B covers the region between 58.75° W and 52.50° W, and 38.20° S and 32.60° S, with a horizontal zonal/meridional resolution of 2.5′/1.75′ (approximately 4 km). Given that the wavelength of the tide is more than 300 km (Simionato et al. 2005) and that the scale of the surge is near to 1000 km (Pugh 2004), a resolution of 4 km is enough to properly solve the processes of interest and provides a reasonable number of grid points describing them throughout the entire area of interest (i.e., FTZ), with at least 10 to 12 points even at its uppermost part (e.g., Simionato et al. 2004a; Luz Clara Tejedor et al. 2015, Moreira and Simionato 2019, Dinàpoli et al. 2020a). Increasing the resolution, in order to provide detailed information about the circulation that may occur in small inlets along the coast or within the ports, would be desirable. Nevertheless, this last will not be possible in the short term due to the lack of data of the bathymetric details in those regions of the RdP, except along the (narrow) navigation channels and in the vicinity and inside the main harbors (Dinàpoli et al. 2020b). The empirical criteria of 1/3 for the resolution reduction from father to child models (Simionato et al. 2006a; Simionato et al. 2006b; Santoro et al. 2011) was used. Bathymetries for both models were built by combining ETOPO2v2 (Amante 2009) dataset with data provided by the Hydrographic Service of the Navy (SHN) for depths shallower than 200 m that come from digitization of nautical charts (SHN 1986, 1992, 1993, 1999a, b). Additionally, floods in the upper half of the FTZ of the RdP occur mainly because the rainfall cannot drain properly due to the level set by the surges more than to inundation; therefore overland flooding was not taken into account.

Model A is forced along its lateral open boundaries by the astronomical tide composed by the 8 principal diurnal and semidiurnal constituents (M_2, S_2, N_2, K_2, K_1, O_1, Q_1 and P_1) provided by the TPXO9 model (Egbert and Erofeeva 2002). Surface and bottom stress tensors are computed through the quadratic parameterization, Eq. 4

$$\boldsymbol{\tau}_S = c_D^w \rho_A w \mathbf{w} \tag{4a}$$

$$\boldsymbol{\tau}_B = c_D \rho_0 u \mathbf{u} \tag{4b}$$

where is c_D^w is the wind drag coefficient, ρ_A is the air density, w is the wind speed, $\mathbf{w}$ is the wind vector, c_D the quadratic bottom friction parameter, ρ_0 is the water density, u is the current speed and $\mathbf{u}$ is the current vector. c_D was

set at 0.002 at every node of both A and B domains. c_D^w was parameterized using the formula proposed by Bowden (1983), Eq. 5:

$$c_D^w = \begin{cases} 1.1 \times 10^{-3} & \text{, for } w < 5 \text{ m s}^{-1} \\ (1.1 + 0.06w) \times 10^{-3} & \text{, for } w \geq 5 \text{ m s}^{-1} \end{cases} \quad (5)$$

Sea level pressure, surface air density and 10-m wind data are the 1-hourly ERA5 (Copernicus Climate Change Service 2017) reanalysis of the European Centre for Medium Range Weather Forecast, with 0.25° spatial resolution.

For the flow of the tributary rivers, daily observations (Borús et al. 2008) are used to set the Paraná and Uruguay rivers discharges (Fig. 1). Both main branches of the Paraná River (Guazú-Bravo and Palmas) were incorporated in the simulations at the upper part of the FTZ as is usual (e.g., Maskell et al. 2014; Dinápoli et al. 2020a). Even though in nature part of the tidal and surge energy might propagate upstream along the tributary rivers, they were not considered in this study. Their inclusion requires specific simulations taking into account the elevation of the terrain and the presence of the Delta of the Paraná River; besides the fact that those areas are beyond the interest of this particular study, high resolution updated bathymetries, which are not fully available yet, would be necessary.

Finally, the time steps of the father and child models are of 15 and 5 s, respectively, consistent with the CFL criterion (Courant et al. 1928). Solutions were saved every 1 h of simulation for the analysis.

To illustrate the satisfactory capability of the model of reproducing the observed water level at the FTZ during the period analyzed in this article, the upper three panels of Fig. 3 shows the model solution (solid red line) superimposed to the observations (black dots) for the tide (η_T, upper panel), the surge (η_S, central upper panel) and the total water level (η, central lower panel), i.e., the combination of the tide, the surge, the CDR and the interactions. Time series correspond to Palermo station (located at MABA, white square in the lower panel). The observed tide was derived from harmonic analysis, whereas the observed surge was calculated as the difference between water level observations and the computed tide. The root-mean-square error ($RMSE$) between simulations and observations is 0.20 m for the tide and 0.27 m for the surge, which corresponds to 13% and 8% of the respectively variability range. The timing can be evaluated through the Pearson correlation factor (R); results for the tide and the surge are 0.75 and 0.88, respectively. The $RMSE$ for the water level is 0.24 m (5% of its variability range) and R is 0.91, being 1 the optimal. This shows the improvement of the numerical solutions when both the tide and the surge are taken into account together in the simulation, because of the inclusion of the interactions in the computation. For comparison of the performance of our model with others in literature, for instance, Dullaart et al. (2020) reported a $RMSE$ normalized by the variability range (or $NRMSE$) of 8% at Florida (USA), Li et al. (2019) got a $NRMSE$ of 14% at Southern China, whereas (Ribeiro et al. 2018) obtained 12% at Brazil. This way, the 8% obtained for our application compares well to state-of-the-art storm surge modeling in other parts of the world, supporting the implementation of the CROCO application presented for the modelization of tides and storm surges in the RdP. Further details about the model development, validation and its particular performance during surges in the FTZ with realistic CDR can be found in Dinápoli et al. (2020b, a).

For the study of the interactions in the RdP we focused on the period spanning between August 15th and December 15th 2010, when two of the most extreme storm surge events of this century occurred in a relatively short period of time. The positive surge event took place between August 30^{th} and September 5^{th} (highlighted in green in the third panel of Fig. 3), when strong and persistent southeasterly winds (fourth left panel of Fig. 3) produced a level anomaly of almost 3.00 m at that station, being 1.60 m the alert level (D'Onofrio et al. 1999). A strong negative surge event took place a bit later, between October 28th and November 3rd (highlighted in blue in the third panel of Fig. 3), when strong winds from the west and west-southwest blew over the RdP (fourth right panel of Fig. 3) and produced a level anomaly about −2.50 m at Palermo station, being −1.20 m the alert level (D'Onofrio et al. 1999). The remaining period (RP) corresponds to that between PSS and NSS, which is not highlighted in Fig. 3. This way, the chosen simulated period permits to study how the surge-CDR interaction develops during both positive and negative extreme events, and also during periods when winds are of intermediate strength. This last was made for comparison between extreme surges and periods characterized by "weaker" positive and negative surges, of no more than approximately 1.50 m (see Fig. 3). The same time period shown in Fig. 3 was considered for the tide-CDR interaction simulations because it is long enough to sample several times the spring-neap cycle of the tide.

Regarding the discharge of the tributary rivers during the simulation analyzed in this work, Fig. 4 shows the flow of the Paraná-Palmas (red), Paraná-Guazú (blue), Uruguay (green) rivers and the total (Q, black) for the period. It can be noted that Q shows relatively little variation along those four months. In addition, during both studied surge events (shaded in green and blue) Q remained almost constant. Based on those observations and on the fact that significant changes in the water level occur for variations of at least

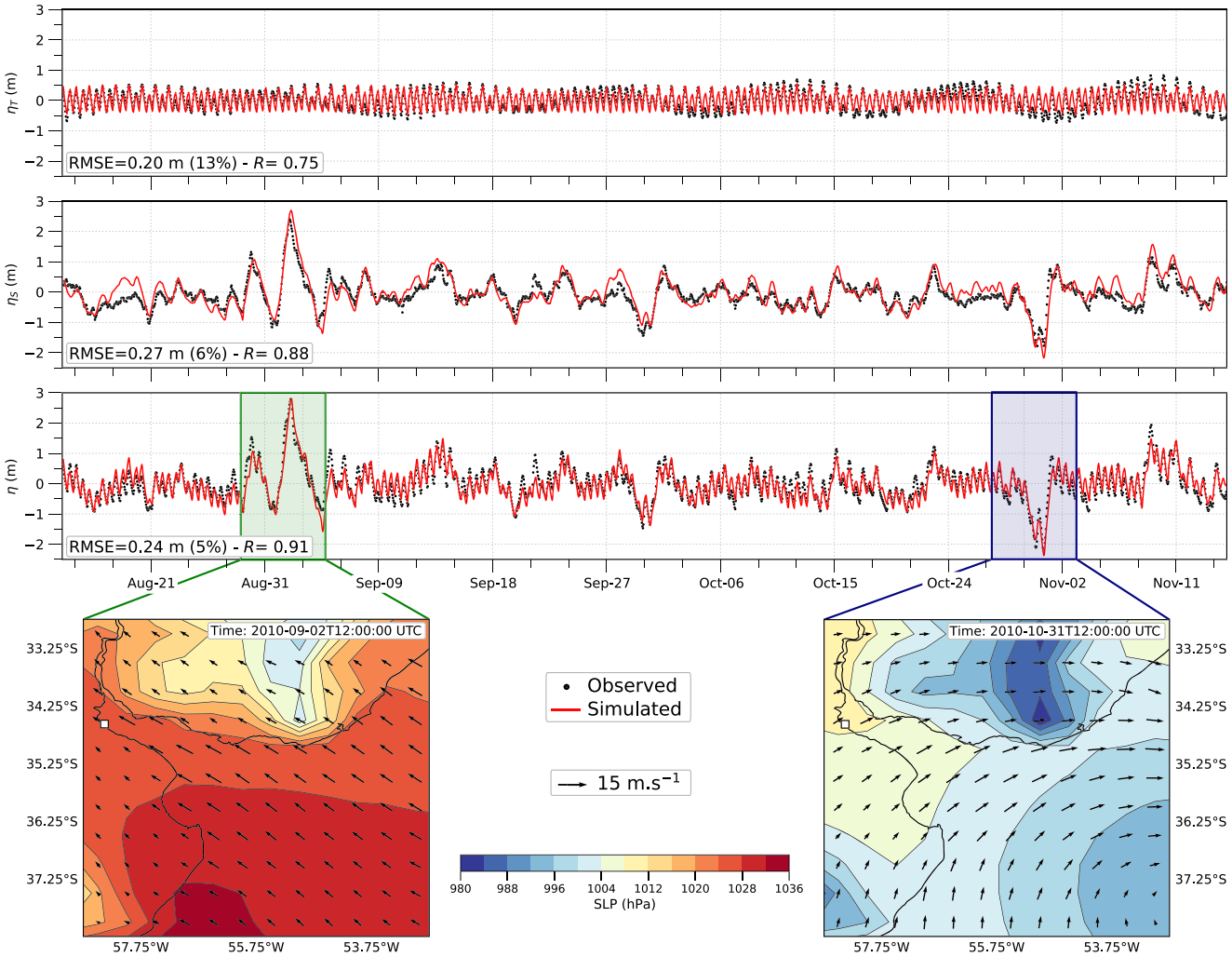

Fig. 3 Model solution (solid red line) and observations (black dots) for: the tide (η_T, upper panel), the surge (η_S, central upper panel) and the total water level (η, central lower panel). The three time series correspond to Palermo station (white square lower panel). In the central lower panel the extreme positive storm surge is highlighted in green, whereas the negative one is highlighted in light blue. Lower panel: surface winds for the moment of the peak of each storm, represented by vectors, and contours of the atmospheric sea level pressure (SLP in hPa). Adapted from Dinápoli et al. (2020c)

one order of magnitude in Q (Dinápoli et al. 2020b), that parameter is set to a constant value during each simulation. This avoids the occurrence of changes in the interactions between CDR, tides and surges that might be confusing for the analysis. The mean Q_{P50} = 22,000 m^3 s^{-1} was chosen unless specified.

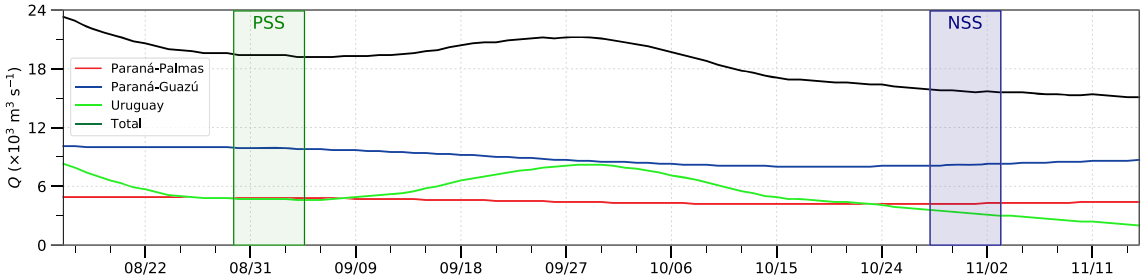

Fig. 4 Discharge of the tributary rivers during the simulated period: Paraná-Palmas in red, Paraná-Guazú in blue, Uruguay in light green and the total continental discharge in black. The orange and blue shades indicate the period when the positive (PSS) and the negative (NSS) storm surge occurred, respectively

Characterization of Nonlinear Interactions in the Numerical Simulations

For the analysis of interactions, we followed the terminology introduced by Wolf (1978), and applied in several papers (e.g., Bijlsma 1986; Bernier and Thompson 2007; Zhang et al. 2010; Idier et al. 2012; Dinàpoli et al. 2020c). Wind waves inside the estuary are usually locally generated (sea) because both short and long swell coming from the Continental Shelf are strongly attenuated by refraction and bottom friction within the FTZ of the RdP (Dragani and Romero 2004). Significant wave heights and periods are relatively low (0.52 m and 3.3 s, respectively) and wave breaking does not often occur (Dragani and Romero 2004); therefore wave-induced setup can be considered negligible for this analysis. This way, the water level (η_{WL}) is considered to be the algebraic sum of (i) the pure tide or surge level (η_T/η_S); (ii) the pure river discharge elevation (η_R); and (iii) the residual elevation due to the nonlinear interactions (η_I), so that, Eq. 6:

$$\eta_{WL} = \eta_{T/S} + \eta_R + \eta_I \tag{6}$$

Using the numerical model, those terms were computed as the solution of simulations with (i) tidal forcing only; (ii) atmospheric forcing only (surface wind and atmospheric pressure); (iii) Q only; and (iv) the full forcing, including tidal/atmospheric and Q forcings. η_I is then calculated as a residual using Eq. 6.

Bijlsma (1986) showed that nonlinear interactions in the shallow waters equation system (Gill 1982; Pedlosky 1987; Zhang et al. 2010) can be related to (i) the advective terms ($(\mathbf{u}\cdot\nabla)\,\mathbf{u}$); (ii) the bottom friction terms (4); and (iii) the shallow waters effect, related to the total depth ($H = h + \eta$, being h the unperturbed depth and η the water level anomaly). To study the possible sources for those interactions in the FTZ of the RdP, another set of simulations was performed straightforwardly "turning off" the above-mentioned effects one at a time as done for instance in Dinàpoli et al. (2020c):

- In the case of advection, CROCO has a flag to deactivate this term in the integrated equation.
- For bottom friction, a linear parameterization instead of the classic quadratic one described above was used following the approach suggested by Zhang et al. (2010). This way, $\boldsymbol{\tau}_B$ is computed as $\boldsymbol{\tau}_{LB} = c_L\rho_0\mathbf{u}$, where c_L is chosen empirically to produce surges with peaks comparable to those predicted by the nonlinear model, i.e., meeting the scales of $\boldsymbol{\tau}_B$ and $\boldsymbol{\tau}_{LB}$ by $c_L \sim c_D\mathbf{u}$. This way, the amount of energy dissipated by bottom friction in both simulations is similar, but in the linear one the interactions are omitted. Figure 5 presents the comparison of the water level at Palermo station (MABA; Fig. 1) derived from simulations forced with nonlinear (black) and linear (red) bottom friction with $c_D = 2.0\times10^{-4}$ and $c_L = 7\times10^{-4}$ ms^{-1}, respectively. Figure 5 shows that the election of cL allows to preserve the order of magnitude of both the tide (upper panel) and the surge (lower panel) and highlights the effects of the nonlinearities: generation of overtides and/or compound tides that modify the shape and the amplitude of the tide and the time evolution of the surge.
- For the case of the shallow waters effect, Eqs. 2 and 3 are linearized using the deep water approximation ($\eta \ll h$), where H is reduced to h.

To provide an estimation of the diverse effects, the differences between the "full" solution and the solution without each one of those effects are presented.

Finally, following others works (for instance, Idier et al. 2012; Dinàpoli et al. 2020c), the absolute maximum value or uniform norm ($\|\cdot\|_\infty = \max(|\cdot|)$) was chosen as a measure of amplitudes and differences. In addition to being equivalent to the other norms, this measure is an upper bound of the root-mean-square distance (Trèves 1967). Therefore, from a practical point of view, the uniform norm is a useful tool to estimate uncertainties.

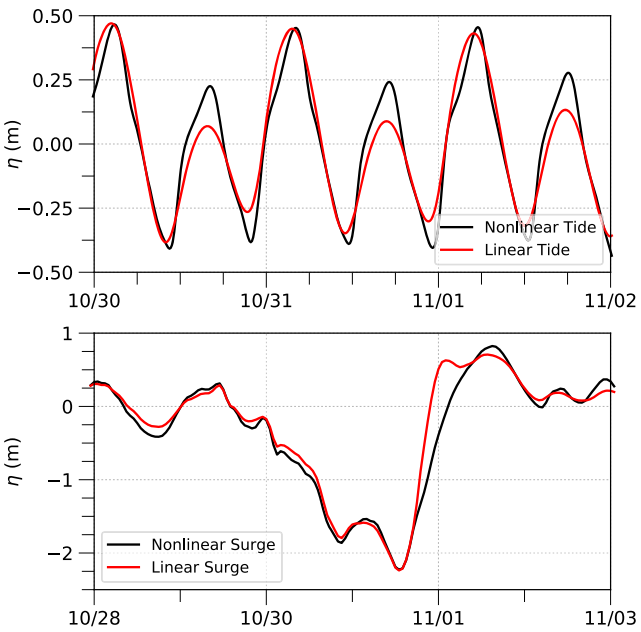

Fig. 5 Comparison of water level at Palermo station, for simulations forced with nonlinear (black) and linear (red) bottom friction for pure tide (upper panel) and pure surge (lower panel)

Results

Observational Evidence of the Occurrence of Tide-CDR and Surge-CDR Interactions in the FTZ of the RdP

Surrogate Analysis

For the study of tide-CDR and surge-CDR interactions the different time scales of variability of the involved processes should be taken into account: Q (seasons to years), tides (hours) and surges (days). For this reason, the analysis of surrogates was carried out for different phases of Q (Fig. 2, bottom panel): (i) "El Niño" period: a trimester of 1983, a Niño year, when Q reached the historical extreme maximum of 87,800 $m^3\ s^{-1}$ (lower left panel); (ii) "La Niña" period: a trimester of 1986, a Niña year, when Q reached an extreme minimum of 10,000 $m^3\ s^{-1}$ (lower central panel); and (iii) "Average" period: an arbitrary trimester with an average Q of 22,000 $m^3\ s^{-1}$ (corresponding to 1994–1995). During the three chosen periods Q remained relatively constant (bottom panel of Fig. 2), and they are long enough to guarantee that several surge events as well as many tidal cycles can be captured.

The analysis of surrogates was applied to tide gauge series collected at Palermo (MABA, located at the upper part of the FTZ) and Oyarvide (located on the outermost portion of the FTZ) stations, shown as a square and a black triangle on the map in Fig. 6. A total of 250 surrogate time series were computed for each series. The upper panel of Fig. 6 shows the distribution of α computed for the surrogates (red box plot) and for the time series of water level at Palermo and Oyarvide (blue circles) during the El Niño (left panel), Average (central panel) and La Niña (left panel) periods. The figure indicates that in both sites there is a significant nonlinear component for the three phases of Q. This interaction might be partially explained by the tide-surge interaction (Dinàpoli et al. 2020c); nonetheless, α computed for the observations decreases as the flow rate does (from left to right in Fig. 4) in Palermo observations, whereas in Oyarvide α remains almost constant for each period. Therefore, the methodology proves statistically the occurrence of a nonlinear component in water level at the upper portion of the FTZ of the RdP due to interaction with CDR, and suggests that nonlinearities become negligible at its outer portion.

To determine whether the interaction observed in the upper panel of Fig. 6 corresponds to tide-CDR interaction, surge-CDR interaction or both, the central and lower panels of Fig. 6 show the results of another subrogate analysis applied to the tide gauge series recorded at Palermo and Oyarvide after applying them low pass (central panel) and high pass (lower panel) filters with cut-off periods of 30 h. Since the tide-surge interaction has the frequency of the tide (Dinàpoli et al. 2020c), the low pass filter at 30 h completely removes that component and isolates surge-CDR interaction. Results for phenomena with periods more than 30 h (central panel of Fig. 6) indicate that surge-CDR interaction is significant only in Palermo (located in the upper part of the FTZ of the RdP) and for average to high Q; for those two cases α of the observations is very close to the box plot but statistically different from α of the surrogates. Also note that α for the low pass filtered signals is always much smaller than α of the non filtered ones (upper panel of Fig. 6). For La Niña (extreme minimum Q), α of the observations is within

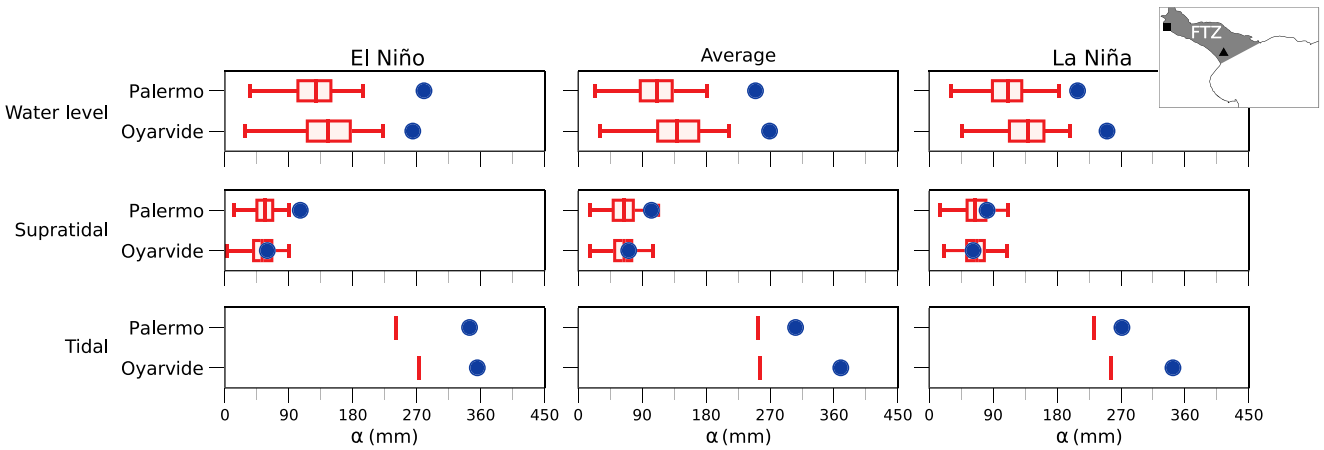

Fig. 6 Time-irreversibility (α, in mm) for Palermo (square) and Oyarvide (triangle) stations during the periods: El Niño (left panel), Average (central panel) and La Niña (right panel). In blue α computed for the observations. In red the boxplots that sintetize α computed for the surrogates. The comparison is made for the total observed water level (upper panel), and the filtered signals for periods more than 30 h (supratidal, central panel) and less than 30 h (tidal, lower panel). The map shows the area of the FTZ of the RdP and the location of the tidal stations

the box plot, indicating that for very low flow rates the interaction (if it occurs) cannot be distinguished from the background noise. In the case of the high pass filtered (tidal) component of the water level series (bottom panel of Fig. 6), α is significant for both stations during the three periods. Although part of this significance can be attributed to nonlinear tide-surge interaction (Dinàpoli et al. 2020c), at Palermo α increases with Q, indicating the occurrence of surge-CDR interaction in the upper portion of the FTZ. At Oyarvide, α is independent of Q, suggesting that, in the external part of the FTZ, surge-CDR interaction is no longer distinguishable.

In summary, the analyses of surrogates suggest that both tide-CDR and surge-CDR interactions develop in the upper part of the FTZ of the RdP and strongly decrease downstream, becoming statistically negligible close to the Barra del Indio Shoal.

Harmonic Analysis

In the particular case of the tide, nonlinearities cause modulations or distortions that can be represented by combining the characteristic or linear constituents (M_2, O_1, S_2, etc.) with an additional set of overtides and compound tides (Parker 2007; Pugh 2004). These nonlinear harmonics develop in shallow regions as a consequence of the nonlinear terms in the shallow waters equations (Parker 2007; Pugh 2004; Gallo and Vinzon 2005): bottom friction, shallow water effect and horizontal advection. This way, the identification of nonlinear harmonic constituents through harmonic analysis provides an alternative method to detect tide-CDR interaction in tide gauge observations. Considering the results of the previous subsection, the harmonic analysis discussed in what follows was performed for the time series of Palermo station for El Niño and La Niña periods (Fig. 2).

When applying harmonic analysis it should be taken into account that, being based on least squares fits, results are very sensitive to the length of the time series. Following the recommendations of Parker (2007), only those constituents that can be solved with a trimester of hourly data (92 days) were considered. To reduce the errors in the estimation of the amplitude and phase of the tidal constituents, the methodology suggested by Luz Clara Tejedor et al. (2014) was followed: before extracting each harmonic, a band pass filter centered on the frequency of interest is applied. This way, the harmonic analysis is applied to monochromatic signals (as many as the number of constituents considered), much less noisy. The filter was a recursive band pass one (Smith 1999), which is characterized by a very narrow bandwidth which is achieved at the expense of the loss of many observations at the extremes of the time series. Therefore, the filter was applied to a long tide gauge series and then the harmonic analysis was applied to the filtered La Niña and El Niño periods. Table 1 shows the amplitudes and phases of the constituents extracted; the horizontal line

Table 1 Harmonic analysis of the time series at Palermo

Constituents	La Niña		El Niño	
	Amplitude (m)	Phase (°)	Amplitude (m)	Phase (°)
M_2	0.262 ± 0.001	302 ± 0	0.249 ± 0.001	302 ± 0
O_1	0.146 ± 0.001	265 ± 0	0.148 ± 0.001	262 ± 0
K_1	0.088 ± 0.002	86 ± 1	0.081 ± 0.001	6 ± 0
N_2	0.087 ± 0.001	264 ± 0	0.092 ± 0.001	261 ± 0
S_2	0.041 ± 0.000	32 ± 1	0.032 ± 0.001	41 ± 1
MN	0.034 ± 0.000	54 ± 0	0.032 ± 0.000	56 ± 0
M_4	0.024 ± 0.001	128 ± 1	0.031 ± 0.001	153 ± 1
$2MN_2$	0.015 ± 0.001	314 ± 2	0.027 ± 0.001	358 ± 1
MS_4	0.012 ± 0.001	196 ± 3	0.008 ± 0.001	230 ± 4
MN_4	0.011 ± 0.001	118 ± 4	0.026 ± 0.001	124 ± 1
MO_3	0.011 ± 0.001	135 ± 3	0.026 ± 0.000	121 ± 0
$2MK_5$	0.008 ± 0.001	73 ± 5	0.006 ± 0.000	85 ± 4
MK_3	0.007 ± 0.001	255 ± 3	0.016 ± 0.001	248 ± 2
M_6	0.007 ± 0.001	301 ± 3	0.005 ± 0.000	312 ± 3
$2MN_6$	0.005 ± 0.001	255 ± 5	0.004 ± 0.001	293 ± 7
$2MS_2$	0.004 ± 0.001	322 ± 8	0.011 ± 0.001	191 ± 2
$2MS_6$	0.004 ± 0.000	47 ± 7	0.002 ± 0.001	38 ± 8
$3MK_7$	0.001 ± 0.000	230 ± 18	0.002 ± 0.001	291 ± 6

The black line divides the linear tidal harmonics from the nonlinear

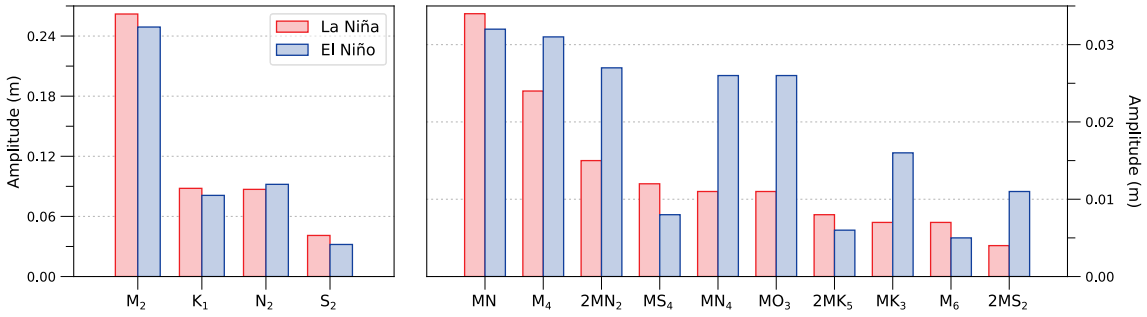

Fig. 7 Comparison of the amplitude of the linear (left panel) and nonlinear (right panel) constituents at Palermo station from La Niña (red) to El Niño (blue) periods

divides the linear constituents (M_2, O_1, K_1, N_2, and S_2) from the nonlinear ones.

The amplitude estimates of the harmonics O_1, $2MN_6$, $2MS_6$ and $3MK_7$ are not significantly different between La Niña and El Niño periods. Nonetheless, significant differences are found for several linear and nonlinear constituents. To favor the interpretation of results, Fig. 7 shows a bar graph of the amplitudes of those constituents for La Niña (in red) and El Niño (in blue) periods. In general, the linear harmonics (left panel) lose amplitude (i.e., energy) as increases. Most of the nonlinear harmonics (right panel) gain energy (M_4, $2MN_2$, MN_4, MO_3, MK_3, $2MS_2$), although some of them lose it (MN, MS_4, $2MK_5$, M_6). In general, Fig. 7 suggests that an increase of Q results in a redistribution of energy among the tidal constituents with a net gain of energy by overtides at the expense of energy of the linear constituents.

To analyze the effect of this reconfiguration of amplitudes, Fig. 8 shows a set of synthetic series constructed as the addition of all the tidal constituents reported in Table 1 for La Niña (red solid line) and El Niño (blue solid line), and the addition of the nonlinear overtides of Table 1 for La Niña (red dashed line) and El Niño (blue dashed line); to compare, the "linear" signal (addition of M_2, O_1, K_1, N_2, and S_2) is shown (black solid line). Figure 8 shows that the nonlinear signals (dashed lines) present a characteristic period equal to half of the fundamental one of 12.42 h, determined by M_2. Although some overtides decrease their amplitude as Q increases, most of them become more energetic (Fig. 7), and thus the amplitude of the nonlinear signal increases for larger Q (dashed blue line). This suggests that the amplitude of the tide-CDR interaction is modulated by the CDR. From the comparison between the total signals (solid red and blue lines) and the "linear" signal (solid black line) it is concluded that the nonlinearities modify the asymmetry of the water level oscillation: the level rise becomes faster and the fall becomes slower (Fig. 8).

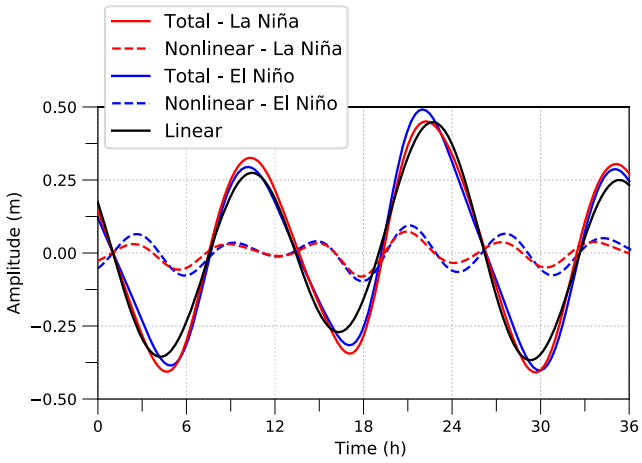

Fig. 8 Synthetic series constructed as the addition of all the tidal constituents reported in Table 1. The solid lines correspond to addition of the linear constituents, whereas the addition of overtides are the dashed lines. Results for La Niña are in red and for El Niño in blue. As reference, the "linear" signal (addition of M_2, O_1, K_1, N_2, and S_2) is in black solid line

Characterization of the Interactions with Numerical Simulations

Tide-CDR Interaction

Figure 9 shows the uniform norm of the water level due to both the tide and Q (η_{WL}, upper left), the pure tide (η_T, upper right), the pure Q (η_R, lower left) and the residual tide-CDR interaction (η_I, lower right), derived from the simulations run for the whole time period shown in Fig. 3. Note that the color scale of every subpanel is different. Figure 9 shows that $\|\eta_{WL}\|_\infty$ is mainly explained by $\|\eta_T\|_\infty$. Both plots (upper panel of Fig. 9) show the characteristic pattern of a Kelvin wave propagating upstream along the southern coast of the channel first, and then exiting the RdP along its northern coast, much weakened because of the dissipation that occurs inside the RdP (Simionato et al. 2005). Maximum values are of the order of 1.10 m at Samborombón Bay and decay to around 0.50 m at the upper part of the FTZ. $\|\eta_R\|_\infty$ displays a tilting of the water level due to the action of the Coriolis force on CDR (deviating to the left in the Southern

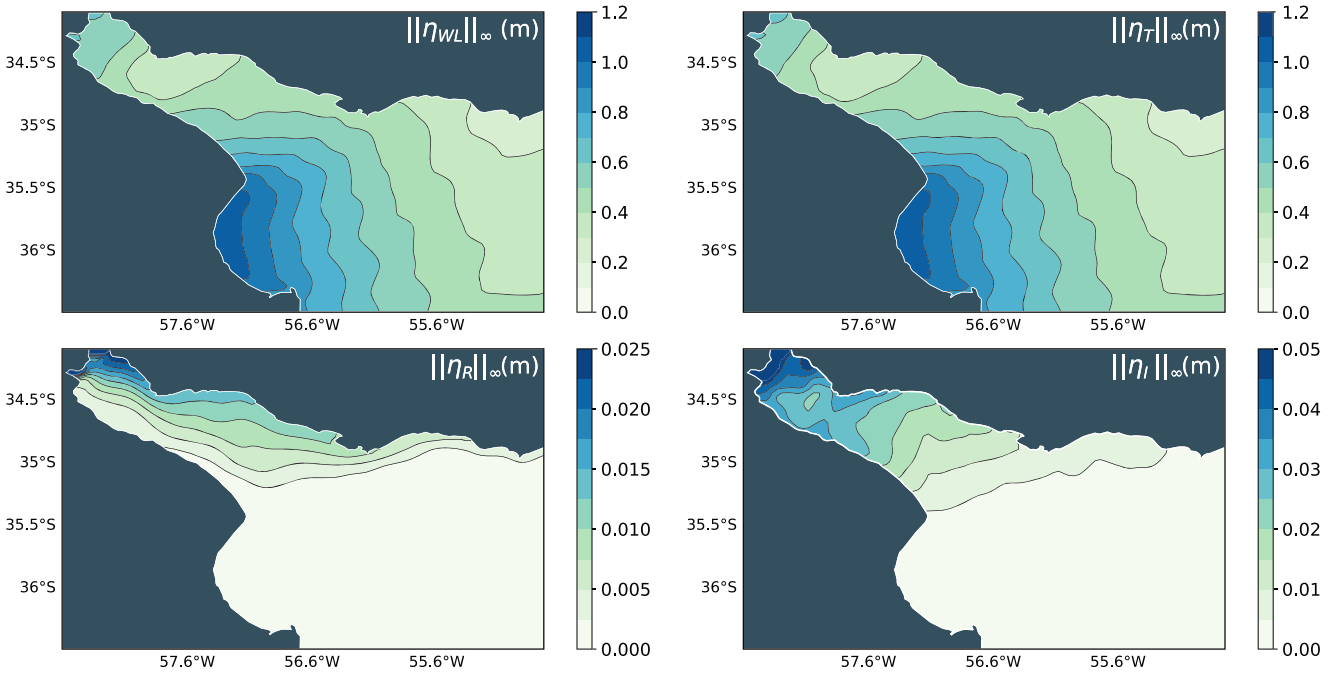

Fig. 9 Uniform norm ($||\cdot||_\infty$ in m) of the total water level anomaly (η_{WL}, upper left panel), pure tide (η_T, upper right panel), pure Q (η_R, lower left panel) and tide-CDR interaction (η_I, lower right panel). Note that the color scale for the residuals is different than for the other plots

Hemisphere), reaching a maximum of almost 0.025 m close to the Uruguay River mouth (Fig. 9). This value is relatively small in spite of the large Q because of the broadness of the RdP (around 40 km at the upper FTZ). Even though $\|\eta_R\|_\infty$ is lower than the $RMSE$ of the numerical model, its correspondence with reliable physics guarantees that this process and the analyses derived from it stand out from the model uncertainties. At the outer part ot the FTZ $\|\eta_R\|_\infty$ becomes almost negligible. $\|\eta_I\|_\infty$ occurs over all the FTZ of the RdP and decreases downstream, as the depth and width of the channel increase. The amplitude of the interaction is twice $\|\eta_R\|_\infty$, being 0.05 m (approximately 12% of $\|\eta_{WL}\|_\infty$) at the upper FTZ, and 0.01 m at its outer part (approximately 1% of $\|\eta_{WL}\|_\infty$). Offshore the Barra del Indio Shoal (outside the FTZ), interactions are negligible.

To analyze the mechanisms for the interactions, the upper panel of Fig. 10 displays the uniform norm of the difference between water level anomalies coming from the nonlinear model simulations (η_{WL}) and the reduced (or linear) model that does not include (i) the quadratic bottom friction ($\|\eta_{BF}\|_\infty = \|\eta_{WL} - \eta_{NoQBF}\|_\infty$, left panel), (ii) the shallow waters effect ($\|\eta_{SWE}\|_\infty = \|\eta_{WL} - \eta_{NoSWE}\|_\infty$, central panel) and (iii) the horizontal advection ($\|\eta_{HAD}\|_\infty = \|\eta_{WL} - \eta_{NoHAD}\|_\infty$, right panel). The upper panel of Fig. 10 shows that the quadratic bottom friction is the dominant term; the largest differences between simulations with linear and nonlinear bottom friction display the same spatial pattern that $\|\eta_I\|_\infty$ (lower right panel, Fig. 9) and, moreover, reach similar values to the interaction anomaly (Fig. 9, lower right panel). The shallow waters effect and the horizontal advection play comparatively a minor role, with their maximal effect at the upper FTZ. It should be mentioned that results are almost independent of the spring-neap cycles of the tide, the interactions changing for only a few millimeters.

To assess the effect of changes in Q, the lower panel of Fig. 10 shows tide-CDR interaction computed from simulations considering (i) a low Q, defined at the first quartile of the historical flow of the tributaries in Q_{P25} = 16,000 $m^3\ s^{-1}$ (left panel); (ii) the mean Q_{P50} = 22,000 $m^3\ s^{-1}$ (central panel); and (iii) a high Q, defined at the third quartile of the historical flow of the tributaries in Q_{P75} = 30,000 $m^3\ s^{-1}$ (right panel). The interquartile range ($Q_{P75} - Q_{P25}$) was chosen because it is the most common, and simplest, robust and resistant measure of spread, also known as dispersion or scale (Wilks 2011). The interquartile range is a good index of the spread in the central part of a dataset, since it simply specifies the range of the central 50% of the data. The fact that it ignores the upper and lower 25% of the data, makes it quite resistant to outliers (Wilks 2011). The lower panel of Fig. 10 shows that increased Q amplifies the amplitude of the interaction, even though its spatial pattern is preserved, with interactions maximizing at the upper FTZ and decaying offshore the Barra del Indio Shoal. The magnitude of the difference between the interaction with Q_{P25} and Q_{P75} (interquartile range) cases at the upper part of the FTZ was 0.03 m. This way, an intensification of

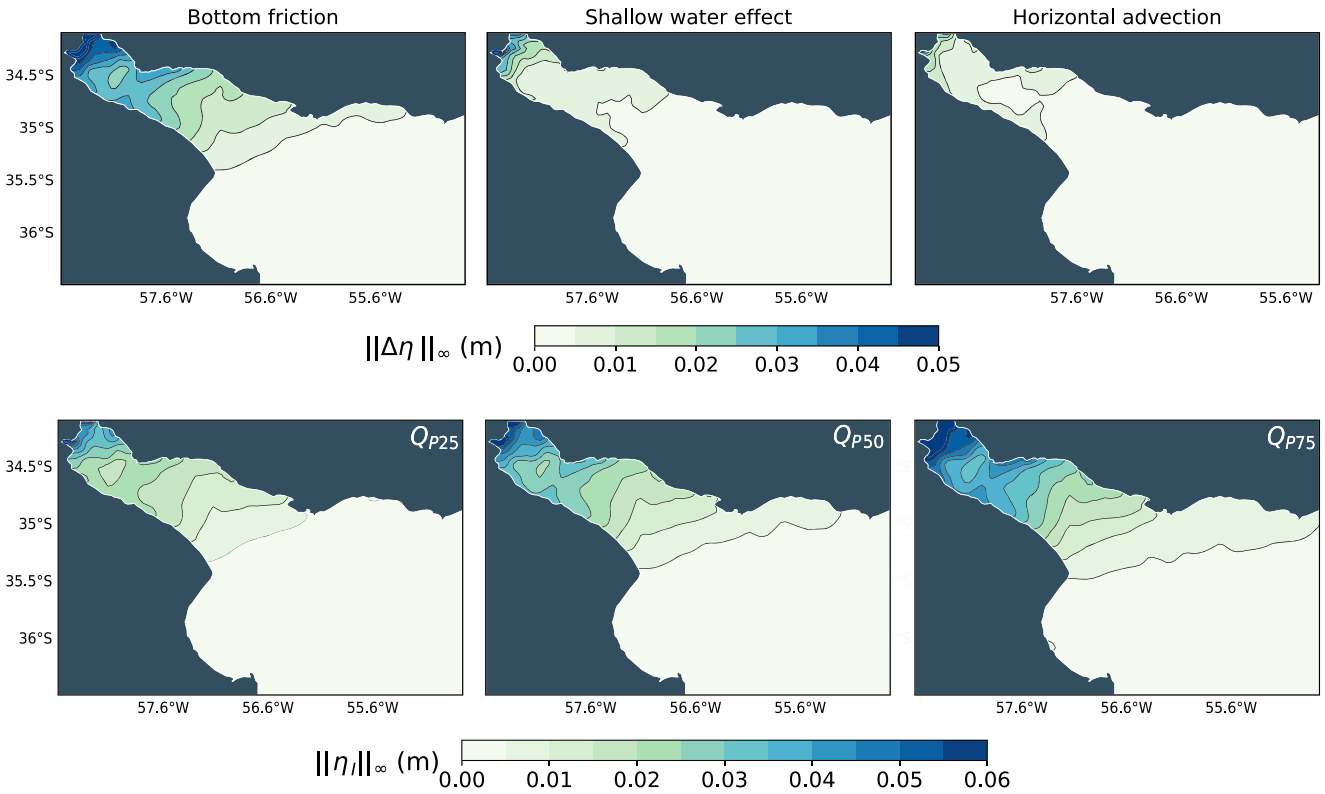

Fig. 10 Upper panel: Uniform norm ($\|\cdot\|_\infty$ in m) of the water level anomaly of the difference ($\Delta\eta$) between simulations including and not including the quadratic bottom friction (left panel), the shallow water effect (central panel) and the horizontal advection (right panel). Lower Panel: tide-CDR interaction for a low ($Q_{P25} = 16,000$ m^3 s^{-1}, left panel), the mean ($Q_{P50} = 22,000$ m^3 s^{-1}, central panel) and a high (Q_{P75} = 30,000 m^3 s^{-1}, right panel) discharge of the tributary rivers

14,000 m^3 s^{-1} in the discharge produces an amplification of the interaction of almost 50%.

Surge-CDR Interaction

Figure 11 shows the uniform norm of the total water level anomaly due to both the surge and Q ($\eta_W L$, left column), the pure storm surge (η_S, central left column), the pure Q (η_R, central right column) and the surge-CDR interaction (η_I, right column), derived from the simulations. The figures were built for three different conditions: (i) PSS (upper panel of Fig. 11): during the positive storm surge period highlighted in red in Fig. 3; (ii) NSS (central panel of Fig. 11): during the negative storm surge period highlighted in light blue in Fig. 3; and (iii) RP (lower panel of Fig. 11): the remaining period, spanning between PSS and NSS. Note that the color scales of the panels are different.

For the three periods, $\|\eta_{WL}\|_\infty$ is mainly explained by $\|\eta_S\|_\infty$. $\|\eta_R\|_\infty$ follows the pattern described in the previous subsection. $\|\eta_I\|_\infty$ is greater than $\|\eta_R\|_\infty$ and shows a similar pattern for the three analyzed periods, with a gradient oriented along the estuary axis, maximizing upstream in the upper portion of the FTZ. For the NSS period the interaction is larger, suggesting that the water depth might play a role in its development. Results, nevertheless, always display a similar pattern, increasing upstream; this suggests that the process that produces the interaction is at independent of the circulation mode (Simionato et al. 2004a, 2006b) excited by the wind direction.

Since the interaction is independent of the sign of the surge (i.e., wind direction) the discussion in what follows considers the whole time period shown in Fig. 3. The upper panel of Fig. 12 presents the uniform norm of the difference ($\|\Delta\eta\|_\infty$) between the interactions from simulations including and not including (i) the quadratic bottom friction (left panel), (ii) the shallow waters effect (central panel) and (iii) the horizontal advection (right panel). The upper panel of Fig. 12 shows that the quadratic bottom friction is the principal source of surge-CDR interaction: the spatial pattern of $\|\eta_I\|_\infty$ (lower right panel, Fig. 11) is similar to the upper left panel of Fig. 12 and reaches comparable amplitudes. The shallow waters effect and the horizontal advection play a comparatively minor role. Nevertheless, both terms have influence on the whole FTZ.

The lower left, central and right panels of Fig. 12 show surge-CDR interaction computed considering low, mean

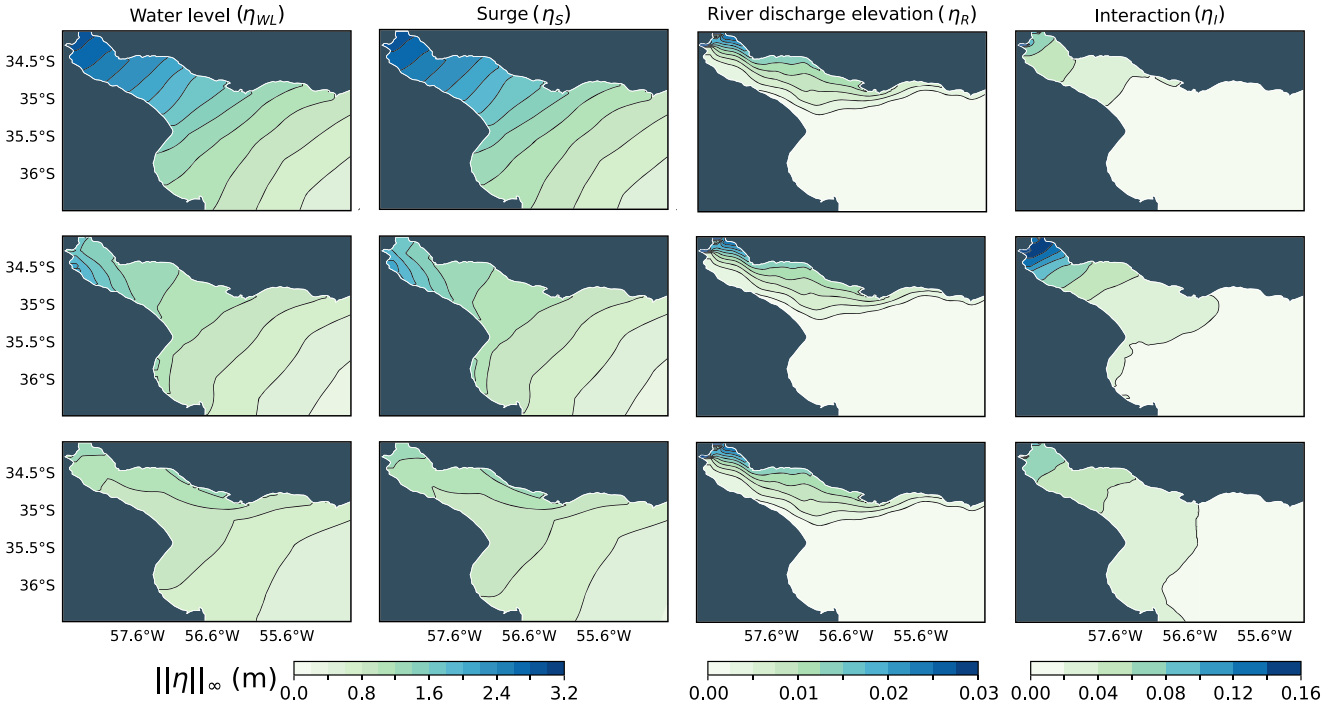

Fig. 11 Maximum absolute values ($\|\cdot\|_\infty$ in m) of the total water level anomaly (η_{WL}, left panel), pure surge (η_S, central left panel), pure Q (η_T, central right panel) and surge-CDR interaction (η_I, right panel) for the period comprised between August 15^{th} and December 1^{st} 2010: positive extreme storm surge (PSS, upper panel), negative extreme surge (NSS, central panel) and remaining period (RP, lower panel) in "normal" conditions

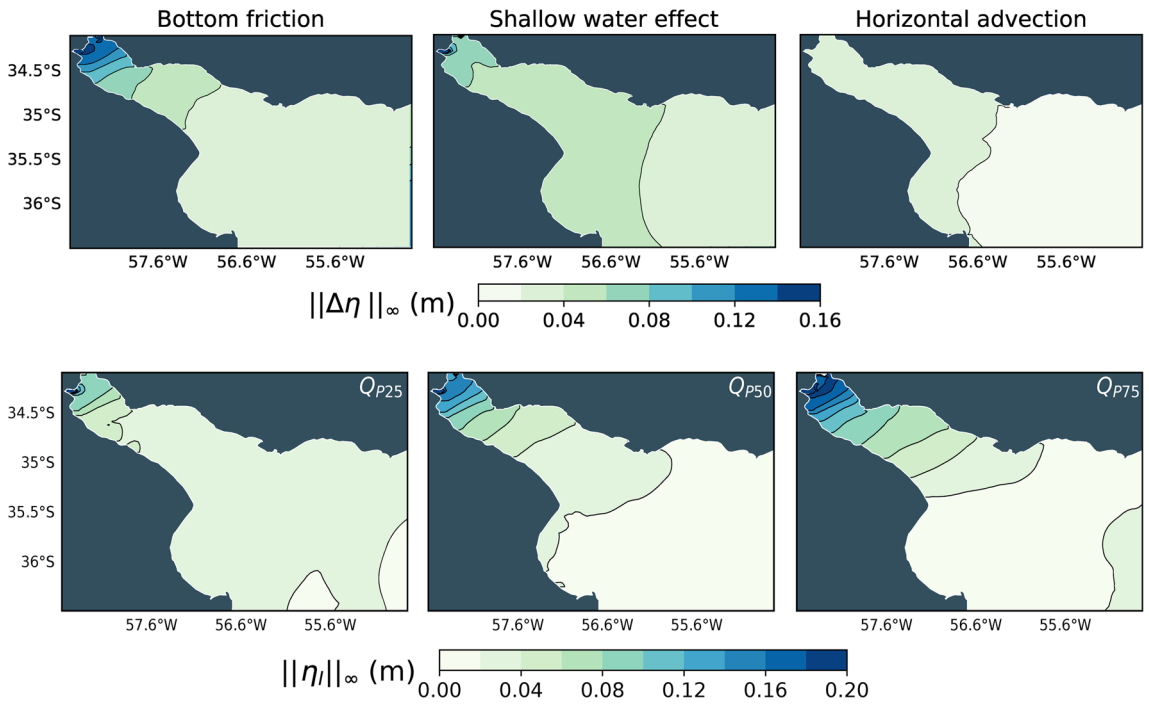

Fig. 12 Upper panel: Uniform norm ($\|\cdot\|_\infty$ in m) of the water level anomaly of the difference ($\Delta\eta$) between simulations including and not including the quadratic bottom friction (left panel), the shallow water effect (central panel) and the horizontal advection (right panel). Lower Panel: surge-CDR interaction for a low ($Q_{P25} = 16,000$ m^3 s^{-1}, left panel), the mean ($Q_{P50} = 22,000$ m^3 s^{-1}, central panel) and a high ($Q_{P75} = 30,000$ m^3 s^{-1}, right panel) river discharge

and high Q, respectively, defined utilizing the first, second and third quartiles (Q_{P25}, Q_{P50} and Q_{P75}), respectively The figure corresponds to the whole period shown in Fig. 3, because it was found that the spatial pattern of the interaction is independent of the period chosen. The lower panel of Fig. 12 indicates that the intensification of Q amplifies the amplitude of the interaction, but preserves its spatial pattern. The amplitude of the interaction from Q_{P25} to Q_{P75} (interquartile range) increases by 0.14 m at the upper part of the FTZ. This way, a difference in Q of 14,000 $m^3\ s^{-1}$ produces an amplification of the surge-CDR interaction of at least 100%.

Discussion

The surrogate analysis applied to tidal observations collected at the FTZ of the RdP revealed that both tide-CDR and surge-CDR interactions occur at its upper part. It also suggested that the amplitude of the interactions correlates with the magnitude of Q (Fig. 6). In addition, harmonic analysis applied to the same time series supported the results obtained with the surrogate analysis for tide-CDR interaction and showed that it increases the asymmetry in the tidal signal, producing faster floods and slower ebbs.

The numerical solutions produced tide-CDR and surge-CDR interactions that are consistent with the results derived from the observations: nonlinear interactions with the CDR do occur in the FTZ. Interactions (Figs. 9 and 11) mainly develop at the upper half of the FTZ, reaching their maxima upstream MABA. Interestingly, in that area the amplitude of the interactions widely exceeds the water level imposed by Q: tide-CDR interaction accounts for 12% of the total water level, whereas surge-CDR interaction accounts for 5%. The spatial pattern of surge-CDR interaction showed to be independent of the surge sign, i.e., of wind direction, whereas tide-CDR interaction is independent of the spring-neap cycle of the tide.

The numerical simulations analyzing the processes that produce the nonlinearities (Figs. 10 and 12) showed that the quadratic bottom friction governs both the tide-CDR and surge-CDR interactions in the FTZ. In what follows, physical arguments will be discussed to explain this result. In order to facilitate the discussion, Fig. 13 shows the mean depth-averaged current (W) from the simulations with pure surge (left panel), pure tide (central panel) and pure Q (CDR, upper right panel), providing information on the spatial pattern and order of magnitude of that variable in the FTZ. Note that the color scale is different for each process. For the surge and the tide, W was computed for the

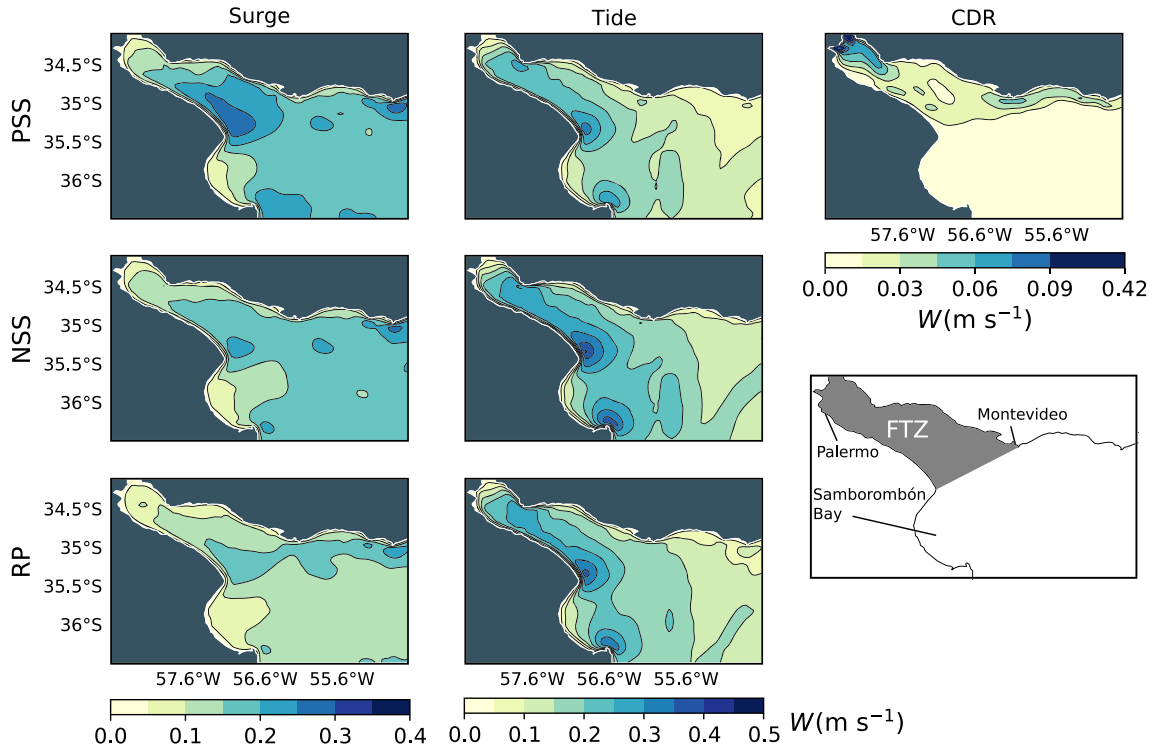

Fig. 13 Mean depth-average current speed (W in ms^{-1}) for the simulations with pure surge (left panel), pure tide (central panel) and pure Q (CDR, upper right panel). W was computed for the period PSS (upper panel), NSS (central panel) and RP (lower panel). Lower right panel: reference for the FTZ (gray shade) and some locations in the RdP. Adapted from Dinápoli et al. (2020c)

three periods PSS (upper panel), NSS (central panel) and RP (lower panel). Figure 13 shows that the spatial structure of the current is, as expected, almost identical for the tide during the three periods, and quite similar for the surge; in this last case the three periods display an intensification at Punta Rasa (uppermost tip of Samborombón Bay; Fig. 13) and the surge current speed is at most half the tidal current speed even for the strongest surge event (PSS, upper panel). This way, the discussion in what follows holds for every period. At the FTZ, tidal currents are stronger along the southern coast, with values up to 0.30 ms^{-1}, whereas along the northern coast speeds are lower (up to 0.20 ms^{-1}). This gradient, transversal to the estuary axis, is due to the tide propagation as a free Kelvin wave; consistently, dissipation is larger along the southern coast than along the northern one (Simionato et al. 2005). Maximum currents occur at the tips of the Samborombón Bay (Fig. 13), with values more than 0.40 ms^{-1}. The mean current speed related to the surge (right panel of Fig. 11) presents a more homogeneous spatial pattern and lower values due to the large scale of the process. Note that, even though the magnitudes of the current are weaker, the associated water level amplitudes are high (Fig. 11) because of the shoaling of the RdP: the channel has a depth of around 50 m and is wide (more than 200 km) offshore the Barra del Indio Shoal, whereas it has a depth of less than 3.00 m and a width of around 40 km at the upper part of the FTZ. Finally, CDR responds to the Coriolis force in the Southern Hemisphere, with a deviation to the left (northern or Uruguayan coast). Downstream the Barra del Indio Shoal, currents attenuate because of the deepening, CDR decaying from 0.10 ms^{-1} at the upper FTZ to 0.06 ms^{-1} close to Montevideo (Fig. 13).

Going back to the discussion of the involved physical barotropic processes, and taking into account the results of Fig. 13, it can be concluded that:

- *Horizontal advection*. The gradients of the currents due to Q, the tide and the surge, are weak. This is the result of the large scale of the RdP, with a total length of 320 km, and a width around 110 km at the Barra del Indio. This is why the horizontal advection ($(\mathbf{u}\cdot\nabla)\mathbf{u}$) is almost negligible.
- *Shallow water effect*. This term depends upon the ratio between the unperturbed water depth (h) and the water level anomaly (η). In this sense, the water level (Figs. 9 and 11) and h become comparable for large surges but not for the tide. During large surges $\|\eta_S\|_\infty$ reaches levels above 2.50 m at the uppermost portion of the FTZ, whereas h is the order of 3.00 m. Therefore, this effect does not occur permanently, but is intermittent.
- *Quadratic bottom friction*. This term, parameterized as $\frac{\boldsymbol{\tau}}{\rho_0 H} = \frac{c_D \|\mathbf{u}\|\mathbf{u}}{H}$, is directly proportional to the square of the total speed, i.e., the algebraic addition of the tidal/surge current and CDR. This way, tide-CDR and surge-CDR interactions maximize at the upper FTZ, where CDR becomes comparable to the tidal/surge current, and both equally contribute to the total quadratic bottom friction. Otherwise, those terms would be associated with the pure tidal or surge currents and they would not involve interactions. Additionally, those terms are amplified for NSS because of the extreme reduction of H at the upper FTZ.

Finally, the strength and the modulation of the interactions due to changes in Q can be explained considering the geometry of the FTZ. Because of the characteristic width and depths, only a large Q can produce a significant variation of CDR. Nevertheless, because of the large range of Q on interannual time scales (from less than 8000 $m^3\ s^{-1}$ during extreme La Niña events, to around 90,000 $m^3\ s^{-1}$ during extreme El Niño events; Fig. 2), a variation of Q in its interquartile range can produce an increment in the interaction amplitude of 50% for the tide and of 100% for the surge.

To complement the analysis, Fig. 14 shows the time evolution of the water level and the interaction at Palermo station (Fig. 1) from numerical simulations for different values of Q. Note that the station is located at the area of maximal interactions (Figs. 9 and 11). The water level (η_{WL}) related to the pure tide (upper panel) and the

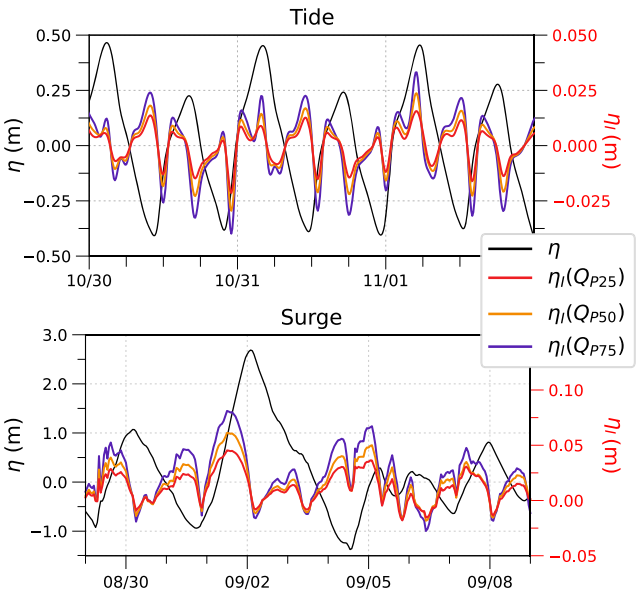

Fig. 14 Time evolution of each component of the water level at Palermo station from the numerical simulations. Water levels (η_{WL} in black) are associated to the left vertical axis. The interactions are referred to the right axis (in red) and correspond to three different river discharges: the first quartile of the river discharge ($\eta(Q_{P25})$ in red), the mean ($\eta(Q_{P50})$ in green) and the third quartile ($\eta(Q_{P75})$ in blue). Upper panel: pure tide. Lower panel: pure surge during the positive extreme surge

pure surge (lower panel) are displayed in black, whereas for the tide-CDR (upper panel) and surge-CDR (lower panel) interactions computed with low ($\eta_I(Q_{P25})$), mean ($\eta_I(Q_{P50})$) and high ($\eta_I(Q_{P75})$) flows of the tributary rivers are presented in red, green and blue, respectively. Note that, because of the difference in their magnitudes, water level is referred to the left vertical axis (in black) whereas the right vertical axis (red) corresponds to interactions; vertical scales differ for the right and left panels of the figure. For the surge-CDR interaction (right panel of Fig. 11), PSS was chosen (period highlighted in green in Fig. 3) because the same conclusions are achieved for NSS. Figure 14 shows that for the tide (upper panel) η_I oscillates with a frequency half of η_{WL}, which is consistent with the intensification of M_4 tidal constituent observed in Figs. 7 and 8. The largest differences occur during the peak-trough transitions of the tide. During the flow, the current due to the tide and CDR are in opposition and then, the total current is weaker and the bottom friction is smaller; as a consequence the rising is faster and the interaction is smaller. During the ebb the reciprocal is valid. This asymmetry in the tidal wave oscillation is indeed observed in data from tidal gauges and was reported by Luz Clara Tejedor et al. (2014). Relatively small changes in the amplitude are observed; nonetheless, the main consequence seems to be mostly on the timing, affecting the shape because the period of the tidal wave cannot change. For surge-CDR interaction (lower panel of Fig. 14), the process is similar: the rising/fall of the level due to the surge, produces currents that are opposed/aligned with CDR. Therefore, the interaction is opposite to the surge time evolution and it is amplified during the peak-through transitions. This last, also, suggests that surge-CDR interaction mainly affects the timing of the surge, slightly accelerating and slowing the risings and the falls, respectively. In both cases, and as expected in terms of the results discussed in the previous section, changes in Q mainly affect the asymmetry of the involved processes.

Conclusions

This work provides observational evidence of the occurrence of nonlinear interactions between the current due to the flow of tributary rivers (CDR), tides and storm surges in the tidal freshwater zone (TFZ) of the Río de la Plata (RdP), which extends between the Barra del Indio Shoal (downstream) and the mouth of the tributary rivers. Those interactions are characterized and quantified using numerical simulations with a regionalized numerical ocean model.

In spite of the fact that the spatial scales of tides and surges are very different, similar conclusions were reached for tide-CDR and surge-CDR interactions. Both maximize at the upper half of the FTZ and significantly vanish downstream. Tide-CDR interaction amplitude reaches 12% of the tidal peak, whereas the surge-CDR interaction is up to 5% of the surge peak. It was also found that a variation of the flow of the tributary rivers (Q) in its interquartile range ($Q_{P75} - Q_{P25}$ = 14,000 $m^3\ s^{-1}$) can amplify the interactions in around 50% and 100% for tide-CDR and surge-CDR interactions, respectively. Even though the interannual variability of Q can be huge in the RdP (up to around 80,000 $m^3\ s^{-1}$ from La Niña to El Niño periods), the increments in the associated CDR and water levels are relatively small because of the strong widening of the channel after the confluence of the tributary rivers; otherwise the effect would be much larger. Interestingly, the spatial pattern of the surge-CDR interaction seems to be quite independent of the wind direction, i.e., is similar for both positive and negative storm surges.

Both tide-CDR and surge-CDR interactions are driven by the quadratic bottom friction. When the tidal or surge waves travel upstream towards the upper FTZ, the associated currents are opposed to CDR; in consequence the total current is lower, the friction (interaction) is lower and the wave rises faster because the period of the wave does not change. On the contrary, when the tidal or surge waves travel downstream from the FTZ head, the associated currents are aligned with CDR; since the current is higher, the friction (interaction) is higher and, therefore, the wave rises slower due to the conservation of the wave period. This process was postulated by Luz Clara Tejedor et al. (2014) for the RdP: in spite of its large width (about 40 km at the upper FTZ) Q is high enough to produce CDR with speeds similar to the tidal current. Finally, it was found that the interaction increases for negative surges as a consequence of the shallow waters effect, i.e., when the water level becomes comparable with the low depths at the upper FTZ.

The conclusions regarding the sources of the tide-CDR interaction are consistent with the results reported by other authors in freshwater tidal zones in other sites of the world. For instance, Alebregtse and de Swart (2016) showed that in the Yangtze Estuary (China) the tide attenuates from the dry to the wet season due to increased friction generated by tide-CDR interaction. Gallo and Vinzon (2005) found that in the Amazon, because of the strong influence of Q, the bottom friction term produces tide-CDR interaction and, moreover, excites overtides over the upper part of the FTZ. Matte et al. (2014) and Jay et al. (2016) showed that nonlinearities due to friction act as a mechanism for compound tides in the St. Lawrence and Columbia River estuaries, respectively. For the Mahakam River (Sassi and Hoitink 2013) found that CDR attenuates the motion of the tide, and that in turn the tide increases friction in the river.

The verification of the occurrence of nonlinear interactions in the FTZ of the RdP highlights the need to reconsider

the tidal analysis techniques, because classical methodologies assume stationary components which may not be adequate to represent the tidal dynamics in that area. In this sense, several methods and improvements have been developed to represent the non-stationary processes of the tide (for instance, the non-stationary harmonic analysis originally developed by Jay and Flinchem (1997, 1999) and Jay and Kukulka (2003). It is foreseen to evaluate the use of those methodologies to RdP tidal records in the near future.

The conclusions of this work provide new insight on the dynamics of the FTZ of the RdP and demonstrate that, from a practical point of view, numerical models for the simulation of the surge and tide in the region must include Q in their architecture. The inclusion of a realistic Q in the simulations can be crucial to adequately produce the temporal evolution and elevation of the water level; in the case of the surge particularly, its duration and moment of the peak. For the RdP, even though the uncertainty in Q (itself low because of the good quality of the observations) does not have a strong impact on the amplitude of the simulated surge (Dinápoli et al. 2020b), surge-CDR interaction can represent up to 5% of the solution of the model. CDR due to Q also interacts with the tide, explaining up to 12% of the tidal peak. This last produces an indirect surge-CDR interaction through the strong tide-surge interaction that develops in the area (Dinápoli et al. 2020c). In conclusion, the storm surge modeling system for the RdP must consider the tide, since it affects the height of the wave peak, and Q, since it affects the peak-to-peak transition speed.

Acknowledgments Matías G. Dinápoli participation was possible thanks to ANPCyT and CONICET PhD fellowships. The authors are grateful to the Instituto Nacional del Agua and the Servicio de Hidrografía Naval for sharing the continental discharge and water level data, respectively. Finally, the authors are also grateful to Reviewer 2 for his or her careful reading of the manuscript and constructive comments and suggestions, which contributed to a significant improvement of this work.

Funding This study was funded by the National Agency for Scientific and Technological Research of Argentina (ANPCyT) PICT 2014-2672 Project, the Programa de Investigación y Desarrollo para la Defensa del MINDEF (PIDDEF) 14-14 Project, and the UBACYT 20020150100118BA directed by Claudia G. Simionato.

Compliance with Ethical Standards

Conflict of Interest The authors declare that they have no conflict of interest.

References

Alebregtse, N, and H de Swart. 2016. Effect of river discharge and geometry on tides and net water transport in an estuarine network, an idealized model applied to the Yangtze Estuary. *Continental Shelf Research* 123: 29–49. https://doi.org/10.1016/j.csr.2016.003.028.

Amante, C. 2009. ETOPO1 1 Arc-Minute Global Relief Model : Procedures, Data Sources and Analysis. National Oceanic and Atmospheric Administration, National Environmental Satellite, Data and Information Service, National Geophysical Data Center. Marine Geology and Geophysics Division.

Balay, MA. 1961. El Río de la Plata entre la atmósfera y el Mar, publicación h-621 edn Servicio de hidrografía Naval. Armada Argentina, Buenos Aires.

Bernier, NB, and KR Thompson. 2007. Tide-surge interaction off the east coast of Canada and northeastern United States. *Journal of Geophysical Research: Oceans* 112.

Bijlsma, AC. 1986. Investigation of surge-tide interaction in storm surge model CSM-16. Delf Hydraulics.

Borús, J, M Uriburu Quirno, and D Calvo. 2008. Evaluación de caudales diarios descargados por los grandes riós del sistema del Plata al estuario del Río de la Plata. Dirección de Sistemas de información y Alerta hidrológico, Instituto Nacional del Agua 154.

Bowden, KF. 1983. *Physical oceanography of coastal waters, Ellis Horwood ltd.* Chichester: Cambridge University Press.

Buschman, FA, AJF Hoitink, M van der Vegt, and P Hoekstra. 2009. Subtidal water level variation controlled by river flow and tides. *Water Resources Research* 45(10). https://doi.org/10.1029/2009wr008167.

Cai, H, Q Yang, Z Zhang, X Guo, F Liu, and S Ou. 2018. Impact of river-tide dynamics on the temporal-spatial distribution of residual water level in the Pearl River channel networks. *Estuaries and Coasts* 41(7): 1885–1903. https://doi.org/10.1007/s12237-018-0399-2.

Campos, EJD, CAD Lentini, JL Miller, and AR Piola. 1999. Interannual variability of the sea surface temperature in the South Brazil Bight. *Geophysical Research Letters* 26(14): 2061–2064. https://doi.org/10.1029/1999gl900297.

Copernicus Climate Change Service. 2017. ERA5: Fifth generation of ECMWF atmospheric reanalyses of the global climate. In: Copernicus climate change service climate data store (CDS). https://cds.climate.copernicus.eu/cdsapp!/home.

Courant, R, K Friedrichs, and H Lewy. 1928. Uber die partiellen differenzengleichungen der mathematischen physik. *Mathematische Annalen* 100: 32–74.

Debreu, L, P Marchesiello, P Penven, and G Cambon. 2012. Two-way nesting in split-explicit ocean models: algorithms, implementation and validation. *Ocean Modelling* 49-50: 1–21.

Dinápoli, MG, CG Simionato, and D Moreira. 2020a. Development and validation of a storm surge forecasting/hindcasting modelling system for the extensive Río de la Plata Estuary and its adjacent Continental Shelf. Natural Hazards. https://doi.org/10.1007/s11069-020-04079-5.

Dinápoli, MG, CG Simionato, and D Moreira. 2020b. Model sensitivity during extreme positive and negative surges in the Río de la plata estuary: Highlighting the need for an appropriate hindcast/forecast system. *Weather and Forecasting* 35(3): 1097–1112. https://doi.org/10.1175/waf-d-19-0171.1.

Dinápoli, MG, CG Simionato, and D Moreira. 2020c. Nonlinear tide-surge interactions in the Río de la Plata Estuary. *Estuarine, Coastal and Shelf Science* 241: 106834. https://doi.org/10.1016/j.ecss.2020.106834.

Dogliotti, A, K Ruddick, and R Guerrero. 2016. Seasonal and inter-annual turbidity variability in the Río de la Plata from 15 years of MODIS: El niño dilution effect. *Estuarine, Coastal and Shelf Science* 182: 27–39. https://doi.org/10.1016/j.ecss.2016.09.013.

D'Onofrio, EE. 1984. Desarrollo de un nuevo sistema de procesamiento de información de marea, informe técnico no. 25 edn Servicio de hidrografía Naval, Buenos Aires, Argentina.

D'Onofrio, EE, MM Fiore, and SI Romero. 1999. Return periods of extreme water levels estimated for some vulnerable areas of Buenos Aires. *Continental Shelf Research* 19(13): 1681–1693. https://doi.org/10.1016/s0278-4343(98)00115-0.

D'Onofrio, EE, MME Fiore, and JL Pousa. 2008. Changes in the regime of storm surges at Buenos Aires, Argentina, (Vol. 24, 260–265. http://www.jstor.org/stable/30133742.

Doodson, AT. 1956. Tides and storm surges in a long uniform gulf. *Proceedings of the Royal Society of London A* 237: 325–343. https://doi.org/10.1098/rspa.1956.0180.

Dragani, WC, and SI Romero. 2004. Impact of a possible local wind change on the wave climate in the upper Río de la plata. *International Journal of Climatology* 24(9): 1149–1157. https://doi.org/10.1002/joc.1049.

Dronkers J. 1986. Tide-induced residual transport of fine sediment. In: Physics of shallow estuaries and bays, american geophysical union, 228–244. https://doi.org/10.1029/ln016p0228.

Dullaart, JCM, S Muis, N Bloemendaal, and JCJH Aerts. 2020. Advancing global storm surge modelling using the new ERA5 climate reanalysis. *Climate Dynamics* 54(1): 1007–1021. https://doi.org/10.1007/s00382-019-05044-0.

Egbert, GD, and SY Erofeeva. 2002. Efficient inverse modeling of barotropic ocean tides. *Journal of Atmospheric and Oceanic Technology* 19(2): 183–204. https://doi.org/10.1175/1520-0426(2002)019<0183:eimobo>2.0.co;2.

Flather, RA. 2001. Storm surges Encyclopedia of ocean sciences, eds. Steele j, S Thorpe, and K Turekian, 2882–2892. San Diego: Academic.

Framiñán, MB, MP Etala, EM Acha, RA Guerrero, CA Lasta, and OB Brown. 1999. Physical characteristics and processes of the Río de la Plata Estuary Estuaries of South America: Their morphology and dynamics, eds. G Perillo, M Piccolo, and MP Quivira, 161–194. Berlin: Springer.

Framiñan, MB, and OB Brown. 1996. Study of the Río de la Plata turbidity front, Part 1: spatial and temporal distribution. *Continental Shelf Research* 16(10): 1259–1282. https://doi.org/10.1016/0278-4343(95)00071-2.

Friedrichs, CT, and DG Aubrey. 1994. Tidal propagation in strongly convergent channels. *Journal of Geophysical Research* 99(C2): 3321. https://doi.org/10.1029/93jc03219.

Gallo, M, and S Vinzon. 2005. Generation of overtides and compound tides in Amazon estuary. *Ocean Dynamics* 55: 441–448. https://doi.org/10.1007/s10236-005-0003-8.

Gill, A. 1982. *Atmosphere-ocean dynamics*, 1st edn. New York: Elsevier.

Godin, G. 1972. *The analysis of tide*. Toronto: University of Toronto Press.

Godin, G. 1985. Modification of river tides by the discharge. *Journal of Waterway, Port, Coastal, and Ocean Engineering* 111(2): 257–274.

Godin, G. 1991. Compact approximations to the bottom friction term, for the study of tides propagating in channels. *Continental Shelf Research* 11(7): 579–589.

Godin, G. 1999. The propagation of tides up rivers with special considerations on the upper Saint Lawrence River. *Estuarine, Coastal and Shelf Science* 48(3): 307–324.

Guerrero, R, M Acha, M Framinan, and C Lasta. 1997. Physical oceanography of the Río de la Plata Estuary, Argentina. *Continental Shelf Research* 17: 727–742. https://doi.org/10.1016/S0278-4343(96)00061-1.

Guo, L, M van der Wegen, DA Jay, P Matte, ZB Wang, D Roelvink, and Q He. 2015. River-tide dynamics: Exploration of nonstationary and nonlinear tidal behavior in the Yangtze River estuary. *Journal of Geophysical Research: Oceans* 120(5): 3499–3521. https://doi.org/10.1002/2014jc010491.

Hoitink, AJF, and DA Jay. 2016. Tidal river dynamics: Implications for deltas. *Reviews of Geophysics* 54(1): 240–272. https://doi.org/10.1002/2015rg000507.

Horrevoets, A, H Savenije, J Schuurman, and S Graas. 2004. The influence of river discharge on tidal damping in alluvial estuaries. *Journal of Hydrology* 294(4): 213–228. https://doi.org/10.1016/j.jhydrol.2004.02.012.

Idier, D, F Dumas, and H Muller. 2012. Tide-surge interaction in the English Channel. *Natural Hazards and Earth System Sciences* 12: 3709–3718. https://doi.org/10.5194/nhess-12-3709-2012.

Jaime, P, A Menéndez, M Uriburu Quirno, and J Torchio. 2002. Análisis del régimen hidrológico de los Ríos paraná y Uruguay Informe LHA 05-216-02 Instituto Nacional del Agua, Buenos Aires, Argentina.

Jay, DA. 1991. Green's law revisited: Tidal long-wave propagation in channels with strong topography. *Journal of Geophysical Research: Oceans* 96(C11): 20585–20598.

Jay, DA, and EP Flinchem. 1997. Interaction of fluctuating river flow with a barotropic tide: a demonstration of wavelet tidal analysis methods. *Journal of Geophysical Research: Oceans* 102(C3): 5705–5720.

Jay, DA, and EP Flinchem. 1999. A comparison of methods for analysis of tidal records containing multi-scale non-tidal background energy. *Continental Shelf Research* 19(13): 1695–1732.

Jay, DA, and T Kukulka. 2003. Revising the paradigm of tidal analysis - the uses of non-stationary data. *Ocean Dynamics* 53(3): 110–125. https://doi.org/10.1007/s10236-003-0042-y.

Jay, DA, AB Borde, and HL Diefenderfer. 2016. Tidal-fluvial and estuarine processes in the Lower Columbia River: II. Water level models, floodplain wetland inundation, and system zones. *Estuaries and Coasts* 39(5): 1299–1324. https://doi.org/10.1007/s12237-016-0082-4.

Jones, JE, and AM Davies. 2008. On the modification of tides in shallow water regions by wind effects. *Journal of Geophysical Research* 113(C5). https://doi.org/10.1029/2007jc004310.

Kim, DH, SJ Hong, HY Lee, DS Kim, YH Jung, HT Kim, and CI Yoo. 2018. Combined effect of river discharge and storm surge on safe water level around urbanized estuary. *Coastal Engineering Proceedings* 1: 96. https://doi.org/10.9753/icce.v36.papers.96.

Kukulka, T. 2003. Impacts of Columbia River discharge on salmonid habitat: 1. a nonstationary fluvial tide model. *Journal of Geophysical Research* 108(C9). https://doi.org/10.1029/2002jc001382.

Lancaster, G, D Iatsenko, A Pidde, V Ticcinelli, and A Stefanovska. 2018. Surrogate data for hypothesis testing of physical systems. *Physics Reports* 748: 1–60. https://doi.org/10.1016/j.physrep.2018.06.001. surrogate data for hypothesis testing of physical systems.

LeBlond, PH. 1978. On tidal propagation in shallow rivers. *Journal of Geophysical Research: Oceans* 83(C9): 4717–4721.

Li, T, F Wang, J Hou, Z Che, and J Dong. 2019. Validation of an operational forecasting system of sea dike risk in the southern Zhejiang, South China. *Journal of Oceanology and Limnology* 37(6): 1929–1940. https://doi.org/10.1007/s00343-019-8240-8.

Losada, MA, M Díez-Minguito, and MÁ Reyes-Merlo. 2017. Tidal-fluvial interaction in the Guadalquivir River Estuary: Spatial and frequency-dependent response of currents and water levels. *Journal of Geophysical Research: Oceans* 122(2): 847–865. https://doi.org/10.1002/2016jc011984.

Luz Clara Tejedor, M, CG Simionato, EE D'Onofrio, MME Fiore, and D Moreira. 2014. Variability of tidal constants in the Río de la

Plata estuary associated to the natural cycles of the runoff. *Estuar Coastal Shelf S* 148(7): 85–96.

Luz Clara Tejedor, M, CG Simionato, EE D'Onofrio, and D Moreira. 2015. Future sea level rise and changes on tides in the Patagonian Continental Shelf. *Journal of Coastal Research* 313: 519–535. https://doi.org/10.2112/jcoastres-d-13-00127.1.

Lyddon, C, JM Brown, N Leonardi, and AJ Plater. 2018. Flood hazard assessment for a hyper-tidal estuary as a function of tide-surge-morphology interaction. *Estuaries and Coasts* 41(6): 1565–1586. https://doi.org/10.1007/s12237-018-0384-9.

Mannattil, M, H Gupta, and S Chakraborty. 2016. Revisiting evidence of chaos in X-ray light curves: The case of grs 1915+105. *The Astrophysical Journal* 833(2): 208. https://doi.org/10.3847/1538-4357/833/2/208.

Mannattil, M, A Pandey, MK Verma, and S Chakraborty. 2017. On the applicability of low-dimensional models for convective flow reversals at extreme Prandtl numbers. *The European Physical Journal B* 90(12): 259. https://doi.org/10.1140/epjb/e2017-80391-1.

Maskell, JH, J Grieser, J Rodney, and NJ Howe. 2016. Investigating typhoon induced river-surge interactions in the Tamsui Estuary, Taiwan. In: American geophysical union, EC34B–1177.

Maskell, J. 2012. Storm surge and river interaction in estuaries, Vol. 5615. In: EGU general assembly conference abstracts.

Maskell, J, K Horsburgh, M Lewis, and P Bates. 2013. Investigating river-surge interaction in idealised estuaries. *Journal of Coastal Research* 30. https://doi.org/10.2112/JCOASTRES-D-12-00221.1.

Maskell, J, K Horsburgh, M Lewis, and P Bates. 2014. Investigating river-surge interaction in idealised estuaries. *Journal of Coastal Research* 294: 248–259. https://doi.org/10.2112/jcoastres-d-12-00221.1.

Matte, P, Y Secretan, and J Morin. 2014. Temporal and spatial variability of tidal-fluvial dynamics in the St. Lawrence fluvial estuary: An application of nonstationary tidal harmonic analysis. *Journal of Geophysical Research: Oceans* 119(9): 5724–5744. https://doi.org/10.1002/2014jc009791.

Meccia, VL, CG Simionato, and RA Guerrero. 2013. The [r]ío de la Plata Estuary response to wind variability in synoptic timescale: Salinity fields and salt wedge structure. *Journal of Coastal Research* 286: 61–77. https://doi.org/10.2112/jcoastres-d-11-00063.1.

Moreira, D, and CG Simionato. 2019. Modeling the suspended sediment transport in a very wide, shallow, and microtidal estuary, the Río de la Plata, Argentina. *Journal of Advances in Modeling Earth Systems* 11(10): 3284–3304. https://doi.org/10.1029/2018MS001605. https://agupubs.onlinelibrary.wiley.com/doi/pdf/10.1029/2018MS001605.

Moreira, D, CG Simionato, F Gohin, F Cayocca, and MLC Tejedor. 2013. Suspended matter mean distribution and seasonal cycle in the Río de la Plata estuary and the adjacent shelf from ocean color satellite (MODIS) and in-situ observations. *Continental Shelf Research* 68: 51–66. https://doi.org/10.1016/j.csr.2013.08.015.

Murty, TS. 1984. Storm surges: Meteorological ocean tides. *Canadian Bulletin of Fisheries and Aquatic Sciences* 212: 897.

Parker, BB. 2007. Tidal analysis and prediction. https://doi.org/10.25607/OBP-191.

Pedlosky, J. 1987. *Geophysical fluid dynamics*, 2nd edn. New York: Springer.

Piola, AR, SI Romero, and U Zajaczkovski. 2008. Space–time variability of the Plata plume inferred from ocean color. *Continental Shelf Research* 28(13): 1556–1567. https://doi.org/10.1016/j.csr.2007.02.013.

Proudman, J. 1955a. The propagation of tide and surge in an estuary. *Proceedings of the Royal Society of London A* 231: 8–24. https://doi.org/10.1098/rspa.1955.0153.

Pugh, D. 2004. *Changing sea levels, effects of tides, weather and climate*. Cambridge: Cambridge University Press.

Re, M, and AN Menéndez. 2011. Modelación hidro-sedimentológica del Río de la plat. dinámica de sedimentos bajo condiciones hidrometeorológicas normales. Proyecto Freplata-FFEM INA-LHA 07-296-11.

Re, M, M Sabarots Gerbec, and AN Menéndez. 2010. Modelación hidro-sedimentológica del Río de la plata. implementación del modelo sedimentológico. Proyecto Freplata-FFEM INA-LHA 06-296-10.

Ribeiro, RB, AFP Sampaio, MS Ruiz, JC Leitão, and PC Leitão. 2018. First approach of a storm surge early warning system for Santos Region. In: Climate change in santos brazil: projections, impacts and adaptation options, 135–157: Springer International Publishing. https://doi.org/10.1007/978-3-319-96535-2_7.

Robertson, A, and CR Mechoso. 1998. Inter-annual and decadal cycles in river flows of southeastern South America. *Journal of Climate* 11: 2570–2581.

Romero, SI. 2008. Estimaciones satelitales de clorofila y los frentes oceánicos del atlántico sudoccidental. PhD thesis, Universidad de Buenos Aires, Facultad de Ciencias Exactas y Naturales.

Rossiter, JR. 1961. Interaction between tide and surge in the Thames. *Geophysical Journal* 6: 29–53. https://doi.org/10.1111/j.1365-246X.1961.tb02960.x.

Santoro, P, M Fernández, M Fossati, G Cazes, R Terra, and I Piedra-Cueva. 2011. Pre-operational forecasting of sea level height for the Río de la Plata. *Applied Mathematical Modelling* 35(5): 2462–2478. https://doi.org/10.1016/j.apm.2010.11.065.

Sassi, MG, and AJF Hoitink. 2013. River flow controls on tides and tide-mean water level profiles in a tidal freshwater river. *Journal of Geophysical Research: Oceans* 118(9): 4139–4151. https://doi.org/10.1002/jgrc.20297.

Savenije, HHG, M Toffolon, J Haas, and EJM Veling. 2008. Analytical description of tidal dynamics in convergent estuaries. *Journal of Geophysical Research* 113(C10). https://doi.org/10.1029/2007jc004408.

Schreiber, T, and A Schmitz. 1996. Improved surrogate data for nonlinearity tests. *Physical Review Letters* 77: 635–638. https://doi.org/10.1103/PhysRevLett.77.635.

SHN. 1986. Mar Argentino, de Río de la Plata al Cabo de Hornos, Carta Náutica 50. Servicio de Hidrografía Naval, Armada Argentina 4° ed.

SHN. 1992. Acceso al Río de la Plata, Carta Náutica H1. Servicio de Hidrografía Naval, Armada Argentina 5° ed.

SHN. 1993. El Rincón, Golfo San Matías y Nuevo, Carta Náutica H2. Servicio de Hidrografía Naval, Armada Argentina 4° ed.

SHN. 1999a. Río de la Plata Exterior, Carta Náutica H113,. Servicio de Hidrografía Naval, Armada Argentina 2° ed.

SHN. 1999b. Río de la Plata Medio y Superior, Carta Náutica H116. Servicio de Hidrografía Naval, Armada Argentina 4° ed.

Simionato, CG, M N Nuñez, and M Engel. 2001. The salinity front of the Río de la Plata - A numerical case study for winter and summer conditions. *Geophysical Research Letters* 28(13): 2641–2644. https://doi.org/10.1029/2000gl012478.

Simionato, CG, WC Dragani, VL Meccia, and M N Nuñez. 2004a. A numerical study of the barotropic circulation of the Río de la Plata Estuary: sensitivity to bathymetry, the earth's rotation and low frequency wind variability. *Estuarine, Coastal and Shelf Science* 61(2): 261–273.

Simionato, CG, WC Dragani, M N Nuñez, and M Engel. 2004b. A set of 3-D nested models for tidal propagation from the Argentinian Continental Shelf to the Río de la Plata Estuary: I. M2. *Journal of Coastal Research* 20(3): 893–912.

Simionato, CG, VL Meccia, WC Dragani, and M N Nuñez. 2005. Barotropic tide and baroclinic waves observations in the Río

de la Plata Estuary. *Journal of Geophysical Research* C06008. https://doi.org/10.1029/2004JC002842.

Simionato, CG, VL Meccia, WC Dragani, R Guerrero, and MN Nuñez. 2006a. Río de la Plata estuary response to wind variability in synoptic to intraseasonal scales: Barotropic response. *Journal of Geophysical Research: Oceans* 111(C9). https://doi.org/10.1029/2005JC003297. https://agupubs.onlinelibrary.wiley.com/doi/abs/10.1029/2005JC003297.

Simionato, CG, VL Meccia, WC Dragani, and M N Nuñez. 2006b. On the use of the NCEP/NCAR surface winds for modelling barotropic circulation in the Río de la Plata Estuary. *Estuar Coast Shelf S* 70: 195–206.

Simionato, CG, VL Meccia, R Guerrero, WC Dragani, and M Nuñez. 2007. Río de la Plata estuary response to wind variability in synoptic to intraseasonal scales: 2. Currents' vertical structure and its implications for the salt wedge structure. *Journal of Geophysical Research* 112(C7). https://doi.org/10.1029/2006jc003815.

Sinha, P, Y Rao, S Dube, A Rao, and A Chatterjee. 1996. Numerical investigation of tide-surge interaction in Hooghly Estuary, India. *Marine Geodesy* 19: 235–255. https://doi.org/10.1080/01490419609388082.

Smith, S. 1999. *The scientist and engineer's guide to digital signal processing*. San Diego: California Technical Pub.

Spicer, P. 2019. Tide and storm surge dynamics in estuaries of variable morphology. Master's thesis, University of Maine. https://digitalcommons.library.umaine.edu/etd/2993.

Trèves, F. 1967. *Topological vector spaces, distributions and kernels*. Amsterdam: Elsevier.

Wankang, Y, Y Baoshu, F Xingru, Y Dezhou, G Guandong, and C Haiying. 2019. The effect of nonlinear factors on tide-surge interaction: A case study of typhoon Rammasun in Tieshan Bay, China. *Estuarine, Coastal and Shelf Science* 219: 420–428. https://doi.org/10.1016/j.ecss.2019.01.024. http://www.sciencedirect.com/science/article/pii/S0272771418305560.

Wilks, D. 2011. Statistical methods in the atmospheric sciences. In: International geophysics: Elsevier. https://books.google.com.ar/books?id=IJuCVtQ0ySIC.

WMO. 2011. *World Meteorological Organization - Guide to storm surge forecasting*. Cambridge: Cambridge University Press. http://hdl.handle.net/11329/393.

Wolf, J. 1978. Interaction of tide and surge in a semi-infinite uniform channel, with application to surge propagation down the east coast of Britain. *Applied Mathematical Modelling* 2: 245–253.

Wolf, J. 1981. Surge-tide interaction in the north sea and river thames. In: Floods due to high winds and tides, 75–94. New York: Elsevier.

Zhang, F, J Sun, B Lin, and G Huang. 2018. Seasonal hydrodynamic interactions between tidal waves and river flows in the Yangtze Estuary. *Journal of Marine Systems* 186: 17–28. https://doi.org/10.1016/j.jmarsys.2018.05.005.

Zhang, WZ, F Shi, HS Hong, SP Shang, and JT Kirby. 2010. Tide-surge interaction intensified by the Taiwan Strait. *Journal of Geophysical Research* 115. https://doi.org/10.1029/2009JC005762.